CHAPTER SIX

Opportunities and challenges in the use of pressure-jump NMR to study Aβ and protein oligomerization

Martin D. Gelenter*, Torry Li[1], Philip Anfinrud, and Ad Bax
Laboratory of Chemical Physics, National Institute of Diabetes and Digestive and Kidney Diseases, National Institutes of Health, Bethesda, MD, United States
*Corresponding author. e-mail address: gelentermd@nih.gov

Contents

[1] Current Address: Department of Pathology and Laboratory Medicine, University of North Carolina, Chapel Hill, NC, United States

Methods in Enzymology, Volume 729
ISSN 0076-6879, https://doi.org/10.1016/bs.mie.2026.01.036

Abstract

Extracellular plaques comprised of amyloid-β (Aβ) are a defining hallmark of Alzheimer's disease. However, it remains debated whether these insoluble fibrils or the soluble oligomers that precede them are the toxic species responsible for pathology. Aβ oligomers are difficult to study by conventional biophysical techniques because of their transient nature and heterogeneous size. While $A\beta_{40}$ oligomers are invisible to solution nuclear magnetic resonance (NMR) spectroscopy due to their slow tumbling, the intrinsically disordered monomeric form is readily detected by solution NMR. Under appropriate conditions, oligomers rapidly form at atmospheric pressure and can be dissociated by the application of ~2.5 kbar hydrostatic pressure. By incorporating pressure jumps within NMR experiments, features of the NMR-invisible oligomers can be probed indirectly by detecting the NMR-visible monomer. This chapter discusses operation of a home-built pressure-jump apparatus and its application to measuring oligomeric relaxation times, chemical shifts, and ^{1}H-^{1}H NOE transfers. $A\beta_{40}$ oligomers have particularly short ^{15}N T_2 relaxation times and long T_1 relaxation times, especially for residues V18-A21 and I31-L34, indicating that these oligomers contain highly ordered regions that tumble slowly in solution. ^{1}H-^{1}H NOEs further reveal that $A\beta_{40}$ oligomers contain hydrogen bonds between V18 and M35, between F20 and G33, and between E22 and I31. Zn^{2+} ions accelerate oligomer formation and promote homogeneous, rigid assemblies with reduced internal motion. Some of the technology development was carried out using Amelotin, an intrinsically disordered protein that also forms pressure-sensitive oligomers but is less prone to irreversible fibril formation and more amenable to large-scale perdeuterated expression.

1. Introduction

Although the presence of extracellular plaques, made up of amyloid-β (Aβ) peptide, and intracellular neurofibrillary tangles, comprised of τ protein, have long been associated with Alzheimer's disease, there is evidence that the soluble oligomers that precede these plaques and neurofibrillary tangles may be a primary toxic species (Blömeke et al., 2024; Tang et al., 2025). These oligomers are believed to exert neurotoxicity through a number of mechanisms involving interaction with cellular membranes and cell-surface receptors. For example, Aβ oligomers have been shown to insert into membranes and form pores which Ca^{2+} ions can pass through, thus disrupting the important calcium homeostasis

in neuron cells (Arispe et al., 1993; Demuro et al., 2011). This dysregulation of cellular calcium homeostasis results in mitochondrial Ca^{2+} overload and subsequent apoptosis (Sanz-Blasco et al., 2008). It has been suggested that oligomers with a lower degree of hydrophobic packing can effectively penetrate cellular membranes and disrupt Ca^{2+} homeostasis (Campioni et al., 2010). Aβ oligomers have also been shown to cause an influx of Ca^{2+} ions into cells through *N*-methyl-D-aspartate (NMDA) and α-amino-3-hydroxy-5-methyl-4-isoxazolepropionic acid (AMPA) receptors by interacting with them and changing the membrane tension, causing mechanical activation of these receptors (Fani et al., 2021). Furthermore, there is evidence for Aβ oligomers promiscuously interacting with cell-surface receptors, triggering a signaling cascade that causes synaptic dysfunction and neurotoxicity (Amin & Harris, 2021).

Consistent with their transient nature, kinetic analyses across multiple amyloid systems show that oligomers most commonly dissociate back to monomers rather than mature into fibrils (Dear et al., 2020), suggesting they are off-pathway to fibril formation. However, transiently high local peptide concentration generated during oligomer dissociation may occasionally promote fibril formation, which in turn can catalyze further oligomer assembly. Indeed, free-energy landscape mapping of $A\beta_{42}$ aggregation shows that secondary nucleation at fibril surfaces is enthalpically favorable and lowers the activation barrier for the formation of new oligomers (Cohen et al., 2018).

Amyloid precursor protein (APP) is proteolytically processed into different Aβ isoforms by β-secretase at the N-terminus and γ-secretase at its C-terminus. Depending on which γ-secretase cleaves the C-terminus, 38–43 residue variants of Aβ are formed (Thinakaran & Koo, 2008). $A\beta_{40}$ and $A\beta_{42}$ are the most prevalent forms, making up ~90 % and a little under 10 %, respectively, of the Aβ found in the brain. While $A\beta_{42}$ is the more cytotoxic isoform (Phillips, 2019), it rapidly aggregates into its fibrillar form even at static high pressure (Ying et al., 2019) and is less amenable to pressure-jump nuclear magnetic resonance (NMR) spectroscopy experiments. For this reason, and the greater proportion of $A\beta_{40}$ found in the brain, the pressure-jump NMR experiments discussed in this chapter focus on $A\beta_{40}$.

If the void volume, ΔV, of a protein, or protein aggregate, is substantially lower in its unfolded state compared to its folded/misfolded state, the protein can be unfolded and/or dissociated with the application of hydrostatic pressure (Foguel et al., 2003; Paladini & Weber, 1981). Because

ΔV increases nearly linearly with oligomer size, larger oligomers experience greater destabilization under pressure and are therefore especially susceptible to dissociation. Pressure denaturation, in contrast to changing the pH, ionic strength, or urea concentration, is a particularly appealing method for studying protein folding and misfolding because it is fully reversible and can be repeated numerous times. Under suitable sample conditions, $A\beta_{40}$ rapidly forms oligomers at atmospheric pressure that can be dissociated in less than a second by applying ~2.5 kbar of hydrostatic pressure (Barnes et al., 2019). While $A\beta_{40}$ oligomers are invisible to solution NMR due to their slow molecular tumbling and associated rapid transverse relaxation, intrinsically disordered monomeric $A\beta_{40}$ yields sharp resonances and is readily detected by solution NMR. By integrating pressure jumps within NMR pulse sequences, features of the NMR-invisible oligomers can be encoded at atmospheric pressure, while detecting the NMR-visible monomeric state at high pressure. This strategy can provide residue-specific information about oligomer structure and dynamics. Oligomers are inherently difficult to study by most other biophysical techniques due to their transient nature and heterogeneous size distributions. For example, exchange rates can be probed using dark-state exchange saturation transfer (DEST) (Fawzi et al., 2011, 2012), chemical exchange saturation transfer (CEST) (Culik et al., 2018), or fluorescence resonance energy transfer (FRET) (Meng et al., 2018; Tosatto et al., 2015), and oligomer interfaces can be identified using paramagnetic relaxation enhancements (PREs) (Karamanos et al., 2015; Kotler et al., 2019). However, atomic resolution details remain elusive with these techniques (Cawood et al., 2021; Chung, 2024).

This chapter begins with the description of a home-built pressure-jump apparatus that can switch the hydrostatic pressure of an NMR sample from atmospheric pressure to ~2.5 kbar on the millisecond timescale (Alderson et al., 2017; Charlier et al., 2018a; Charlier et al., 2018c; Gelenter et al., 2024; Masoumzadeh et al., 2024). It then goes on to describe how sample conditions are optimized for the study of $A\beta_{40}$ oligomers via pressure-jump NMR spectroscopy. These optimal sample conditions are then used to measure ^{15}N T_1 and T_2 relaxation times of $A\beta_{40}$ in the oligomeric state (Barnes et al., 2019). The effects of Zn^{2+} on oligomeric ^{15}N T_1 relaxation times are also investigated. Pressure-jump NMR techniques used to measure chemical shifts and nuclear Overhauser enhancements (NOEs) in the oligomeric state were developed using amelotin (Chiliveri et al., 2023). Amelotin is another protein that rapidly oligomerizes at atmospheric

pressure and can be dissociated with hydrostatic pressure but can survive more than one hundred thousand pressure cycles before forming pressure-resistant aggregates and thus served as a model system for the development of new pressure-jump NMR experiments used to study oligomeric assemblies. Subsequent application of these methods to $A\beta_{40}$ will be shown to pose more severe challenges than encountered for amelotin because their faster growth of oligomer size results in heterogeneous spin diffusion.

2. Operating the pressure-jump apparatus

2.1 Pressure-jump apparatus hardware

A commercial high-pressure NMR accessory, manufactured by Daedalus Innovations (Ashton, PA, USA), is capable of ramping the hydrostatic pressure of an NMR sample from atmospheric pressure up to 3 kbar over a duration of a few minutes (Peterson & Wand, 2005). Although this system is of great utility in studying the equilibrium and pressure dependence of many proteins (Caro & Wand, 2018; Gelenter & Bax, 2023; Kamatari et al., 2004; Roche et al., 2017), it cannot switch between atmospheric pressure and elevated pressures of ~2.5 kbar on the timescales necessary to study protein folding, misfolding, and oligomerization, all of which often occur on the millisecond to seconds timescale (Dill & Chan, 1997; Dyson & Wright, 2017; Gelenter et al., 2024). Kalbitzer and coworkers built a pressure-jump apparatus that can switch from atmospheric pressure to 0.8 kbar in 30 ms, but this system does not reach pressures capable of unfolding many proteins and does not have the level of temporal resolution we desired (Kremer et al., 2011). We therefore sought to build an apparatus capable of rapidly switching the hydrostatic pressure between atmospheric pressure and ~2.5 kbar on a timescale of a few milliseconds or less. In multiple respects, our pressure-jump apparatus shares features with the original Daedalus equipment, including its sample tube, a moderately customized titanium high-pressure adapter that connects the sample cell to the stainless tubing, as well as the tubing itself. For this reason, we named our system Icarus, the mythological son of Daedalus. This home-built pressure-jump apparatus (Fig. 1) relies on mineral spirits or oil as a hydraulic fluid with a density lower than water to transduce the pressure to the NMR sample (Alderson et al., 2017; Charlier et al., 2018a). The non-miscibility of water and mineral oil or spirits prevents the requirement for a physical barrier at the interface between the hydraulic fluid and the sample

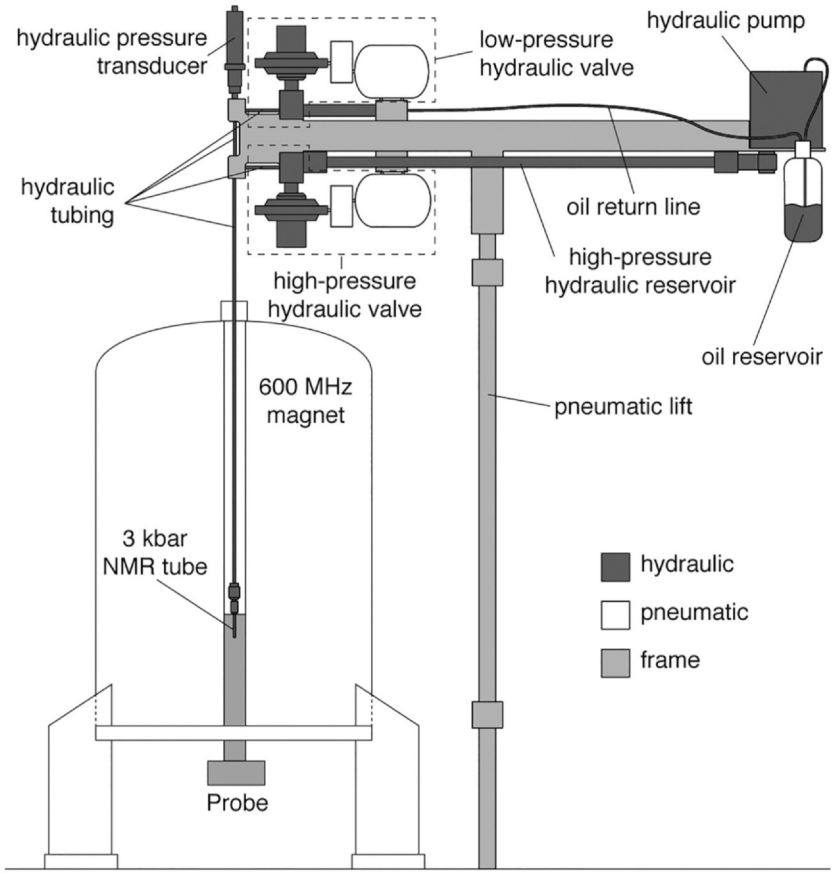

Fig. 1 Schematic representation of the pressure-jump apparatus interfaced with a 600-MHz magnet. The NMR sample is contained within a zirconia high-pressure cell, rated for 3 kbar of hydrostatic pressure. A 1.0-mm inner diameter stainless steel transfer line connects the cell to a manifold with two valves. One valve leads to a reservoir at atmospheric pressure kept under an N_2 atmosphere, while the other connects to a 125 mL stainless-steel reservoir with mineral spirits at a pressure of ~2.5 kbar. The cylindrical geometry of the high-pressure reservoir allows higher pressures than spherical or other reservoir designs. The valves can be operated and the pump can be turned on or off by either the spectrometer or with the Icarus graphical user interface (GUI) that is run on a tablet connected to the pressure-jump apparatus. The hydraulic pump recycles decompressed mineral spirits or mineral oil back into the high-pressure reservoir. The pneumatic valves and reservoirs are mounted atop a pneumatic lift that is used to place the sample into the magnet such that the high-pressure tube is properly seated within the NMR probe. *Reprinted with permission from Charlier, C., Alderson, T. R., Courtney, J. M., Ying, J., Anfinrud, P., & Bax, A. (2018). Study of protein folding under native conditions by rapidly switching the hydrostatic pressure inside an NMR sample cell. Proceedings of the National Academy of Sciences, 115(18), E4169–E4178. https://doi.org/10.1073/pnas.1803642115.*

solution. An important advantage of using mineral spirits rather than mineral oil, which is recommended for the Daedalus syringe pump, is its lower viscosity, which shortens the time required to change pressure, and its high volatility, which obviates the need for cleanup following a leak. Leaks will inevitably occur during mechanically taxing pressure cycling. If the cryoprobe becomes contaminated with high-purity mineral spirits, the fluid evaporates without residue. In contrast, if contaminated with mineral oil, the probe must be removed from the magnet and thoroughly cleaned.

The NMR sample is first loaded into a zirconia high-pressure cell rated for up to 3 kbar of hydrostatic pressure (Peterson & Wand, 2005). This high-pressure tube, manufactured by Daedalus Innovations, is the same tube used on Daedalus Innovation's high-pressure NMR accessory. The currently available variant of the Daedalus high-pressure tube has an outer diameter (OD) of 5 mm and inner diameter (ID) of 2.6 mm and fits into standard 5-mm Bruker NMR probes. The high-pressure tube is attached via a custom high-pressure titanium adapter to a 1.0-mm ID stainless steel transfer line that is filled with mineral spirits. This transfer line is connected via a manifold to two valves: one valve is connected to a return reservoir at atmospheric pressure while the other valve is connected to a 125-mL high-pressure reservoir with mineral spirits pressurized to ~2.5 kbar by a pneumatically driven hydraulic pump. The hydraulic pressure is amplified relative to the applied air pressure by the ratio of the cross-sectional areas of the reciprocating piston, which for the MaxPro L400-VES pump (Fairview, PA, USA) is approximately 400:1. Note that we employ pneumatically operated pumps and valves to avoid the pitfalls of operating electrically driven equipment near the strong magnetic fields generated by our unshielded NMR magnets. By opening and closing the pneumatic valves, the pressure of the NMR sample can be rapidly switched between atmospheric pressure and high pressures up to 2.5 kbar. At 2.5 kbar the aqueous sample is compressed by about 8 % while the mineral spirits are compressed by about 12 %. When the valve going to the atmospheric pressure reservoir is opened, the mineral spirits expand into the return reservoir, after which they are recycled into the high-pressure reservoir by the hydraulic high-pressure pump. Prior to operation, it is important to purge the lines to avoid gas bubbles. If gas bubbles contain oxygen, adiabatic heating of the gas during rapid pressurization triggers combustion and formation of soot that contaminates and darkens the hydraulic fluid and NMR sample after a few thousand pressure cycles. To prevent this detonation, the entire hydraulic system is kept under an atmosphere of nitrogen.

Pressurizing the aqueous NMR sample from atmospheric pressure to 2.5 kbar leads to an adiabatic temperature increase of about 2.5 K (Masoumzadeh et al., 2024), while dropping the pressure from 2.5 kbar to atmospheric pressure similarly leads to the same temperature decrease. Because mineral spirits are more compressible and have a lower heat capacity than water, its temperature change is much greater than that experienced in the aqueous phase. Moreover, when viscous fluid travels through narrow-bore tubing at velocities approaching the speed of sound, frictional heating, particularly near the valve end of the transfer line, can be significant. After a jump to high pressure, the heated fluid equilibrates with the temperature of the stainless steel transfer line and cools, decreasing its volume and modestly decreasing the sample's hydrostatic pressure. This pressure drop can be mitigated by briefly opening the high-pressure valve a second time. To limit damage to the cryoprobe and magnet following a catastrophic burst of the high-pressure NMR sample cell, the valve connecting the manifold to the high-pressure reservoir is never opened for more than eight milliseconds at a time, such that a worst-case scenario failure only releases the fluids and energy stored in the manifold and tubing, not that of the entire high-pressure reservoir. Moreover, the short duration for which the valve is opened minimizes the valve pin displacement to less than 1 mm, strongly reducing wear on the pin and its surrounding packing material, which functions as a leak-free, high-pressure sliding seal.

The initial implementation of this pressure-jump apparatus utilized a 2-mm inner diameter transfer line, which could jump the pressure from 10 to 90 % of the setpoint in about 1 ms. Such a fast change in hydrostatic pressure may at first seem appealing, but it quickly causes mixing and emulsification of the mineral spirits and aqueous buffer solution. Emulsification arises from turbulent flow: the solvent front moves at a linear velocity of ~3.4 m/s, which at 293 K results in a Reynolds number of about 9000, well into the turbulent regime for fluid flow. Shrinking the bore of the transfer line to 1.0 mm slows down the fluid flow and reduces the Reynolds number sufficiently to remain in the laminar regime, which limits mixing of mineral spirits with the sample at the aqueous interface and prolongs the lifetime of pressure-jump samples.

Decreasing the inner diameter of the transfer line to 1.0 mm increased the time required to pressurize from 10 to 90 % of the target pressure to ~1.6 ms. Although this pressure change was slower than for the 2.0 mm transfer line, it still resulted in an overshoot of the pressure followed by an oscillation in the pressure for ~15 ms, analogous to water hammer in a

home plumbing system. This oscillation can also contribute to turbulent mixing of the mineral spirits with the aqueous sample. A titanium pinhole restrictor with a diameter of 0.13 mm was inserted into the titanium high-pressure adapter to further slow the change in pressure. The inclusion of this pinhole restrictor increased the time required to go from 10 to 90 % of the target pressure to 3.6 ms and dampened the oscillations in pressure. No mixing of the mineral spirits and buffer has been observed with such a pinhole restrictor in use. It takes slightly longer to depressurize the sample: without the pinhole restrictor it takes 4.4 ms to go from 90 to 10 % of target pressure, while with the pinhole restrictor this time increases to 7.4 ms.

As mentioned above, pressurization and depressurization lead to significant frictional heating in the transfer line, within the valves, and in the hydraulic pump, which impact the stability of the pressure. To prevent frictional heating from building up to high values, which would cause pressure instability, a relatively long recycle delay of 9 s is utilized when jumping between atmospheric pressure and 2.5 kbar. For experiments that do not require 2.5 kbar, a faster repetition rate can be used; for example, for 2 kbar, a 6-s interscan delay suffices.

2.2 Pressure-jump apparatus software and interface with NMR spectrometer

The pressure-jump apparatus can be controlled by both the Bruker NMR spectrometer and a standalone tablet or laptop running in-house developed software dubbed Icarus (Fig. 2). The Icarus software is written in python and can be found on GitHub (https://github.com/SeanIFitch/icarus_v2) (Fitch, 2024, 2025). To control the pressure-jump apparatus via the spectrometer, transistor-transistor logic (TTL) signals are utilized. These TTL commands can be incorporated into pulse sequences to control different aspects of the pressure-jump apparatus. The operational state of the pressure-jump apparatus is defined by four bits in the "setrtp0" command, which is embedded in the Bruker NMR pulse sequence. These four bits, which correspond to pressurize, depressurize, pump, and log, are programmed to be active low, which allows the state of the system to be controlled by either the spectrometer or the standalone tablet/laptop running the Icarus control software. Pulling bit 0 low triggers opening of the pressurization valve and resetting it high triggers its closure. Similarly, bit 1 controls the depressurization valve. The pneumatic pump is turned on/off by bit 2, and dataset logging is enabled by bit 3. Suitable TTL commands are inserted

into the NMR pulse sequences to properly synchronize operation of the pressure-jump apparatus. This allows the user to essentially use pressure jumps and pressure drops as another channel within their NMR pulse sequences. When operating the pressurization and depressurization valves, the time between TTL trigger events and valve openings is typically on the order of 20 ms, as recorded by the Icarus software (Fig. 2). Once time delays are known for opening and closing of the high- and low-pressure valves, the user needs to account for this lag time and time the "setrtp0" commands within the pulse sequence accordingly.

The Icarus control software relies on communication with a DATAQ DI-4108 USB device (Akron, Ohio, USA). Once the software recognizes this device, it reads data from seven analog and four digital channels at a rate of 4 kHz. The digital channels monitor the state of the four bits used to control the apparatus. The analog channels monitor the target pressure, the hydrostatic pressure at the manifold side of the transfer line, and if the NMR sample cell is replaced with a pressure sensor for diagnostic purposes, the hydrostatic pressure at the sample end of the transfer line. The time-dependent change in pressure at the sample location is delayed and slower than that measured at the manifold and is influenced by the length and diameter of the transfer line, as well as whether a flow-restrictive pinhole

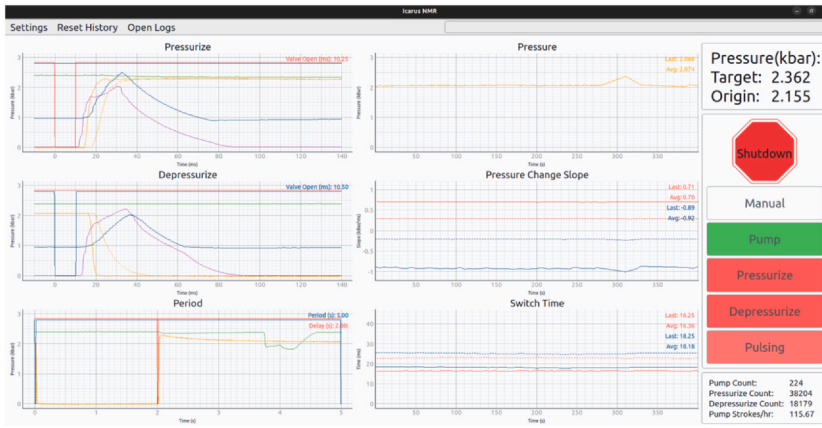

Fig. 2 Example screenshot of the Icarus software graphical user interface (GUI) used to monitor the pressure-jump apparatus. The Icarus GUI contains plots that allow the user to monitor the time it takes to switch pressure, the performance of the valves, and how stable the sample pressure is during the course of a pressure-jump experiment. Additionally, there are buttons on the right side that allow for the manual operation of the pump and valves.

has been inserted into the titanium high-pressure adapter. The most recent implementation of the pressure-jump apparatus utilizes home-built, fully pneumatic pressurization and depressurization valves. Instead of using a properly tensioned compression spring to keep the valve in its normally closed state, the valves were reengineered to use gas pressure in the upper chamber to keep the valve closed. When the sudden rush of pressurized gas in the lower chamber generates pressure that exceeds that in the upper chamber, the valve opens. When exhausting the pressure in the lower chamber, the valve closes. To monitor the performance of these fully-pneumatic valves, the analog channels track the pressure in both upper and lower chambers.

The Icarus control software monitors the pressure-jump apparatus and updates the charts shown in Fig. 2 according to six event handlers. The pressurize event handler detects high-to-low state transitions in the pressurization valve control digital channel. The depressurize event handler detects high-to-low state transitions in the depressurization valve control digital channel. The period event handler detects consecutive high-to-low state transitions in the depressurization valve control digital channel, which define the time range for the Period chart. The pressure event handler detects the current pressure at the manifold side of the transfer line. The pneumatic pump event handler monitors the air pressure on the line connected to the pneumatic pump. When the reciprocating pump reaches the end of its stroke, it makes a return stroke that consumes a significant volume of gas, causing a drop in the pressure feeding the pump. This modulation in pressure is detected, processed, and increments the Pump Count found in the bottom right corner in Fig. 2. The log event handler detects state changes in the log control digital channel, and when pulled low, all events are written to a log file named according to the timestamp corresponding to the start of the experiment. When the experiment is complete, bit 3 is set high and the log file is closed. After the experiment is finished, the GUI can load the log file and the operating performance can be reviewed event-by-event.

The Icarus GUI (Fig. 2) displays six plots that allow the user to monitor the behavior of the pressure-jump apparatus. A 150-ms time interval is plotted for each pressurization and depressurization event. Below these two plots is the period plot, whose range is slightly longer than the time between consecutive depressurization events and reveals the behavior over a full depressurization/pressurization cycle. Multiple signals are overlayed in these plots. The state of the digital channels controlling the

pressurization and depressurization valves are plotted in red and blue, respectively. The target pressure, which is a multiple of the air pressure delivered to the pneumatic pump, is plotted in green and the pressure at the manifold side of the transfer line is plotted in orange. When a pressure sensor is connected in place of the NMR sample, an orange dotted line is plotted which indicates pressure at the sample end of the transfer line. Note that the pressure changes are slower at the sample end compared to the manifold end of the transfer line, in particular when a flow restrictor is in place to slow down the pressure changes. The pressurization and depressurization plots also include pressure in the upper (blue) and lower (magenta) chambers of the pneumatic valves. These traces allow the user to monitor the performance and switching times of the pneumatic valves.

Three additional plots show the running average pressure since the current log file was started, the pressure change slope, and the switching time. The pressure plot is useful for checking whether the pressure-jump apparatus reaches the same pressure throughout an entire experiment. For example, changes in the pressure-change slope can be indicative of a small leak somewhere in the system. The switch-time plot displays how long it takes from the time the TTL command is sent to open the pressurization or depressurization valve until the pressure has reached the midpoint of its pressure transition. This information is used to properly time the TTL commands within a pulse sequence. Variations in the switch time can be indicative of a sticky or failing valve.

On the right side of the GUI (Fig. 2), real-time values for the target pressure (~400-fold higher than the air pressure driving the pump) and the pressure at the top of the transfer line (denoted as the origin) are displayed in units of kbar. Below these fields is a "shutdown" button which turns off the hydraulic pump and briefly opens both the pressurization and depressurization valves to equilibrate the entire system at atmospheric pressure. Buttons that control the operating state of the pump, the pressurization valve, the depressurization valve, and whether the system is in pulsing mode are found below the "shutdown" button. The "pulsing" mode is typically used to test the system and make sure everything is working properly before starting a pressure-jump NMR experiment. The pump count, pressurization event count, depressurization event count, and the number of pump strokes per hour are all listed at the bottom right of the GUI and are particularly useful to keep track of the serviceable lifetimes of the pneumatic valves and pump.

Operation of the pressure-jump apparatus is monitored by a Sentry module, whose warnings are displayed at the top right of the GUI (Fig. 2). If the pump stroke counter increments too quickly during a preset span of time, which is symptomatic of a major leak, the Sentry module shuts down the pump. The Sentry module also monitors the high-pressure achieved following each pressurization event and its stability. If the pressure drops slowly but beyond the expected value due to fluid cooling, the Sentry module generates a warning, but if the drop exceeds a preset threshold, the Sentry module executes a shutdown procedure, which shuts down the pneumatic pump and releases the manifold pressure, thereby stopping the flow of mineral spirits out of the leak and reverting to a safe, unpressurized state.

3. Optimal oligomeric $A\beta_{40}$ sample preparation for pressure-jump NMR experiments

3.1 Preparation of oligomeric $A\beta_{40}$ Samples

^{15}N-labeled $A\beta_{40}$ was either purchased from Alexotech (https://www.alexotech.com) or prepared using previously published protocols (Barnes et al., 2019; Ying et al., 2019). First, ~1.4 mg lyophilized ^{15}N-labeled $A\beta_{40}$ was dissolved in 160 μL of a basic 25 mM KOH solution on ice (Barnes et al., 2019). Then a premixed buffer containing 16 μL 250 mM HCl and 40 μL 350 mM potassium phosphate, pH 6.0, was added to the sample. The HCl in this premixed buffer neutralizes the KOH and the resulting pH is determined by the potassium phosphate buffer. The final concentration of $A\beta_{40}$ was ~1.3 mM. $A\beta_{40}$ rapidly oligomerizes and aggregates under acidic conditions at high concentrations (Schützmann et al., 2021). Indeed, while gently pipetting the solution in and out of the vial to thoroughly mix it, the sample rapidly becomes cloudy as large oligomers are formed.

To limit the buildup of pressure-resistant aggregates, it is crucial to pressurize the sample as quickly as possible once the pH has been dropped by the addition of the phosphate buffer solution. The sample was promptly pipetted into a prechilled high-pressure NMR cell (Peterson & Wand, 2005). Because gel loading pipette tips do not reach the bottom of the high-pressure NMR cell, the sample was pipetted into the cell in one-third aliquots followed by a quick spin in a hand-cranked centrifuge to achieve bubble-free loading of the sample. Mineral spirits were then added on top of the sample to fill the high-pressure NMR sample cell to its rim before a final quick spin in the hand-cranked centrifuge and then attached to a

titanium head connected to the transfer line on the pressure-jump apparatus. After attachment, the apparatus is typically briefly pressure-tested at 2.5 kbar for leaks outside of the magnet, followed by insertion of the assembly into the magnet and bringing the sample up to 2.5 kbar, where the $A\beta_{40}$ is stably monomeric.

3.2 Optimal sample conditions to probe oligomeric $A\beta_{40}$ via pressure-jump NMR

At neutral or basic pH, $A\beta_{40}$ is slow to oligomerize. For probing the oligomerization processes of $A\beta_{40}$ with pressure-jump NMR spectroscopy, the oligomerization must occur on a time scale that is fast relative to the longitudinal relaxation (T_1) of the nucleus of interest (Charlier et al., 2018a). For the relaxation experiments described in this chapter, that nucleus is ^{15}N. Intrinsically disordered proteins (IDPs), such as monomeric $A\beta_{40}$, have a ^{15}N T_1 of ~600 ms on a 600-MHz spectrometer at room temperature (Abyzov et al., 2016). Large, slowly tumbling, well-ordered species, such as crystalline solids without large amplitude internal motions, can have ^{15}N T_1's of many seconds or longer (Cole & Torchia, 1991; Schanda et al., 2010). As discussed in Section 4, very long ^{15}N T_1 values were observed for the most hydrophobic regions of $A\beta_{40}$. The long T_1's associated with $A\beta_{40}$ oligomers can be used to filter signals from such oligomeric species against a large background of fast relaxing monomeric species. For this purpose, a maximum fraction of the monomer population needs to be converted into oligomers before the monomer signal has significantly decayed due to T_1 relaxation. Therefore, conditions must be chosen where a significant proportion of $A\beta_{40}$ oligomerizes within ~600 ms.

The rate at which $A\beta_{40}$ oligomerizes is a function of pH, concentration, and temperature. Lowering the pH, increasing the $A\beta_{40}$ concentration, and increasing temperature all significantly accelerate the rate of oligomerization. After a single pressure cycle, worm-like oligomers are observed (Fig. 3B). Unfortunately, accelerating the rate of oligomerization is also correlated with accelerating the rate at which pressure-resistant fibrils are produced (Fig. 3C). Indeed, after a lag phase of ~2000 pressure cycles, $A\beta_{40}$ monomer intensity rapidly drops (Fig. 3A), indicating the formation of pressure-resistant fibrils that have a short, stubby appearance when viewed by transmission electron microscopy (TEM) (Fig. 3C) and which do not significantly dissociate at 2.5 kbar, even on the time scale of multiple days (Barnes et al., 2019). Only the intrinsically disordered monomeric state of $A\beta_{40}$ is visible to solution NMR, which at high pressure includes

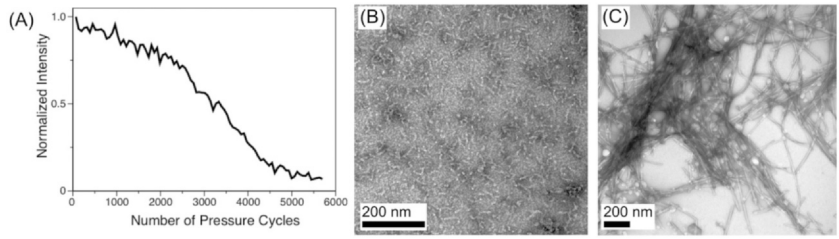

Fig. 3 Loss of monomer $A\beta_{40}$ intensity leads to the buildup of pressure-resistant fibrils. A) Normalized intensity of the amide signals collected 9.8 s after a pressure jump to 2.5 kbar when pressure cycling between 2.5 kbar (10 s) and atmospheric pressure (5 s). B) Negatively stained TEM image of an $A\beta_{40}$ sample that was put on the grid after one pressure cycle. C) Negatively stained TEM image of an $A\beta_{40}$ sample that was put on the grid after 12,000 pressure cycles. *Adapted with permission from Barnes, C. A., Robertson, A. J., Louis, J. M., Anfinrud, P., & Bax, A. (2019). Observation of β-amyloid peptide oligomerization by pressure-jump NMR spectroscopy. Journal of the American Chemical Society, 141(35), 13762–13766. https://doi.org/10.1021/jacs.9b06970.*

the population of oligomers that can be reversibly unfolded with pressure. Therefore, the drop in amide signal intensity after a number of pressure cycles (Fig. 3A) appears to be analogous to the buildup of fluorescence signal in ThT kinetics experiments on $A\beta_{40}$. These fibrils decrease the available monomer concentration that is achieved at high pressure when the oligomers are dissociated, which in turn slows down the oligomerization process after a subsequent pressure drop and thereby decreases the amount of detectable signal. Therefore, selecting the pH, $A\beta_{40}$ concentration, and temperature is a delicate balance between how fast the peptide oligomerizes and how many pressure cycles the sample lasts before a significant fraction converts into pressure-resistant fibrils.

$A\beta_{40}$ samples in pH 6.0 phosphate buffer at a concentration of 1.3 mM and at 293 K offered favorable conditions with relatively fast oligomerization (Fig. 4A), while still surviving enough pressure cycles needed for recording 2D NMR spectra (Fig. 3A). Intrinsically disordered $A\beta_{40}$ monomers yield intense solution NMR signals, while the large, slowly tumbling oligomers are NMR-invisible. The conversion from monomer to oligomer can therefore be easily tracked by collecting 1D NMR spectra. Simple 1D observation of the $A\beta_{40}$ methyl group signals showed that 400 ms after a pressure drop the amount of remaining monomer signal had decayed by ~40 % (Fig. 4A,C), meaning that a significant fraction of the monomer population had been converted to oligomers on a time scale that is shorter than the ^{15}N T_1 relaxation of intrinsically disordered monomers.

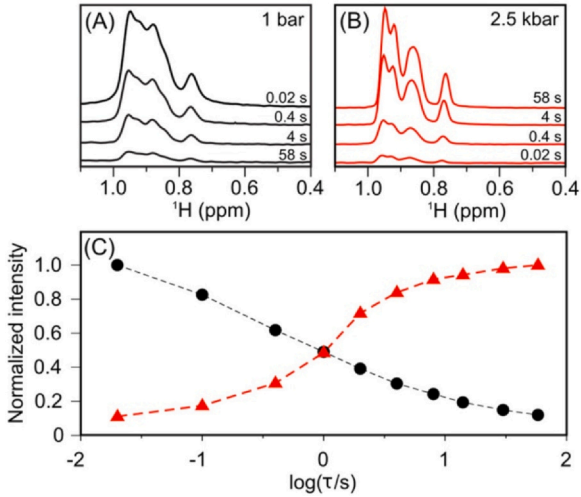

Fig. 4 Signal loss and gain after a pressure drop or pressure jump, respectively. The sample contained 1.3 mM $A\beta_{40}$ in pH 6.0 phosphate buffer at 293 K. (A) Loss of monomer methyl signal after a pressure drop from 2.5 kbar to atmospheric pressure. The sample was equilibrated for 30 s at 2.5 kbar prior to the pressure drop. (B) Gain of monomer methyl signal after a pressure jump from atmospheric pressure to 2.5 kbar. The sample was equilibrated for 30 s at atmospheric pressure before the pressure jump occurred. (C) Integrated methyl signals after a pressure drop (black) or pressure jump (red). *Reprinted with permission from Barnes, C. A., Robertson, A. J., Louis, J. M., Anfinrud, P., & Bax, A. (2019). Observation of β-amyloid peptide oligomerization by pressure-jump NMR spectroscopy. Journal of the American Chemical Society, 141(35), 13762–13766. https://doi.org/10.1021/jacs.9b06970.*

The monomer signal continues to decay with time, although the rate of decay decreases with the decreasing amount of free monomer (Fig. 4C).

Just as the oligomerization process needs to be fast relative to ^{15}N T_1 relaxation, the dissociation or "melting" of oligomers also needs to be fast relative to T_1 relaxation to ensure that enough signal is recovered for detection after the oligomeric species has been dissociated. After spending 30 s at atmospheric pressure, the vast majority of $A\beta_{40}$ monomer has been converted to oligomer. When the pressure is jumped up to 2.5 kbar, the growth of monomer signal, or the decay of the oligomer population, appears roughly exponential (Fig. 4B,C), with about half of the monomer signal being recovered after one second (Fig. 4C). The optimal "melting" time in terms of signal-to-noise then is a balance between how much of the monomer population has been recovered and how much signal is lost due to ^{15}N T_1 relaxation.

4. Measurement of oligomeric $A\beta_{40}$ ^{15}N T_1 relaxation

4.1 Pulse sequence

The pulse sequence for measuring ^{15}N T_1 relaxation times in the oligomeric state (Fig. 5) begins with a refocused INEPT at high pressure to generate in-phase $N_{\pm Z}$ magnetization. The pressure is then dropped to atmospheric pressure for a variable duration, τ, to allow the monomeric $A\beta_{40}$ to oligomerize. During this low-pressure period, the amide protons are inverted at $\tau/4$ and $3\tau/4$ to minimize the extent to which cross-correlated ^{15}N T_1 relaxation of the remaining monomeric species affects the effective ^{15}N T_1. Removal of cross-correlated relaxation effects is important because the TROSY component of the monomeric signal has a relatively long ^{15}N T_1 that can exceed one second. To keep the water

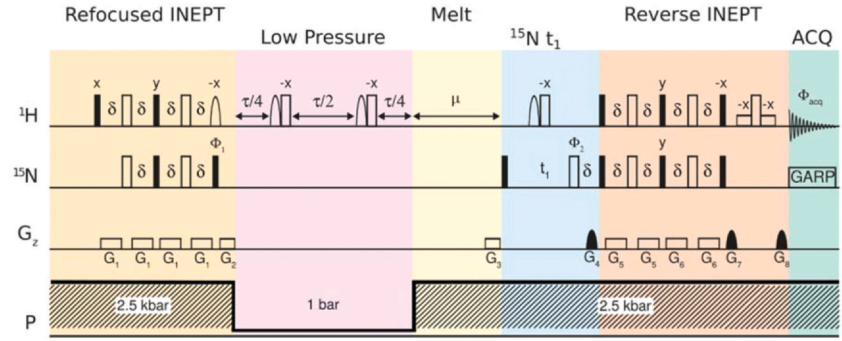

Fig. 5 Pulse sequence for measuring ^{15}N T_1 relaxation times in the oligomeric state (Barnes et al., 2019). Filled and open rectangles on the ^{1}H and ^{15}N radiofrequency channels represent hard 90° and 180° pulses, respectively. The first shaped pulse at the end of the refocused INEPT represents a selective 90° pulse applied to the water resonance. The remaining shaped pulses represent selective inversion pulses applied to the water resonance, as are the weak rectangular 90° pulses that are part of the standard WATERGATE (Piotto et al., 1992) element. Unless otherwise stated, all pulse phases are x. Composite-pulse decoupling on the ^{15}N channel was used during t_2 acquisition using a GARP (Shaka et al., 1985) scheme. The INEPT delays, δ, were 2.7 ms. Phase cycling: $\varphi_1 = \{y, -y\}$, $\varphi_2 = \{x, x, y, y, -x, -x, -y, -y\}$, $\varphi_{acq} = \{x, -x, -x, x\}$. Pulsed field gradients are either sine-bell shaped ($G_{4, 7, 8}$), or weak rectangular ($G_{1, 2, 3, 5, 6}$). Gradient durations and peak amplitudes are as follows: G_1, 2.6 ms, 1.8 %; G_2, 2.0 ms, 15.6 %; G_3, 1.0 ms, 6.2 %; G_4, 2.0 ms, 29.6 %; G_5, 2.6 ms, 0.7 %; G_6, 2.6 ms, 0.5 %; G_7, 0.5 ms, 18.0 %; G_8, 0.5 ms, 30.0 %, where a gradient strength of 100 % corresponds to 53 G/cm. *Reprinted with permission from Barnes, C. A., Robertson, A. J., Louis, J. M., Anfinrud, P., & Bax, A. (2019). Observation of β-amyloid peptide oligomerization by pressure-jump NMR spectroscopy. Journal of the American Chemical Society, 141(35), 13762–13766. https://doi.org/10.1021/jacs.9b06970.*

magnetization along the +z axis, thus preventing adverse effects from radiation damping, selective ^{1}H 180° pulses centered on the water resonance are placed immediately prior to the hard ^{1}H 180° inversion pulses. Following the low-pressure period, τ, the pressure is jumped back to ~2.5 kbar for a "melting" period, μ, in which the $A\beta_{40}$ oligomers are allowed to dissociate back into the intrinsically disordered monomer. The optimal length of the "melting" period delay is a balance between what fraction of the oligomeric species converts back to monomer and how much ^{15}N T_1 relaxation decreases the amount of signal left at the end of the melting period. The μ delay was empirically optimized to be ~350 ms. Following the melting period, the ^{15}N t_1 dimension is evolved prior to a reverse INEPT for a gradient-enhanced HSQC read-out (Kay et al., 1992), including a WATERGATE (Piotto et al., 1992) element for water suppression. To minimize the effects of temperature change and vibration from the pressure jump, the time between the pressure jump and signal acquisition is kept constant. This is achieved by decrementing μ as the ^{15}N t_1 delay is incremented.

Intrinsically disordered peptides at room temperature have a ^{15}N T_1 of approximately 600 ms (Abyzov et al., 2016), while highly-ordered, slowly-tumbling oligomers can have ^{15}N T_1's of many seconds. Therefore, when τ is set to a relatively long delay of 5.5 or 8 s, only magnetization from peptides in the oligomeric state survives this low-pressure delay. Conversely, if the low-pressure delay is set to a time much shorter than the ^{15}N T_1 of monomeric $A\beta_{40}$, e.g. 200 ms, the majority of in-phase magnetization generated at the end of the refocused INEPT will survive the low-pressure period.

Only two interleaved datasets can be collected on an individual sample before the buildup of pressure-resistant fibrils adversely affects the oligomerization and data acquisition. Therefore, a two-point interleaved measurement of the ^{15}N T_1 was conducted with τ delays of 5.5 and 8 s. The ^{15}N T_1's of the oligomeric species were then calculated by assuming the T_1 decay of their signals is monoexponential. After the interleaved ^{15}N T_1 measurement was completed, a reference spectrum with a short τ of 200 ms was collected. This reference spectrum's intensity was then scaled relative to the interleaved dataset by the intensity of its isolated V40 amide H^N signal, obtained from just the first increment of an experiment where three τ values were interleaved, 0.2, 5.5, and 8 s, prior to the start of the 2D HSQC spectra.

The 2D HSQC readout spectra for the ^{15}N T_1 measurements were collected with a 14-ppm spectral width and 120-ms acquisition time in the direct ^{1}H dimension, while a 21.9-ppm spectral width and 75-ms acquisition time were used in the indirect ^{15}N dimension. This leads to a total of 400 FIDs being collected for the interleaved ^{15}N T_1 measurement. With eight scans per FID, the total number of pressure cycles was 3200 and the monomer signal decayed to about half of its original intensity. The $\tau = 200$ ms reference spectrum was collected with the same spectral width and acquisition times, but with only two scans per FID as it is a much higher sensitivity experiment.

4.2 Interpretation of oligomeric $A\beta_{40}$ ^{15}N T_1 relaxation

When the low-pressure delay, τ, was set to 200 ms, which is much shorter than the ^{15}N T_1 of intrinsically disordered monomeric $A\beta_{40}$, all of the resonances, except for the N-terminal D1, were observed (Fig. 6B). However, when τ was lengthened to 5.5 s, a very different spectral pattern emerged which lacked all N-terminal residues spanning A2-G9 (Barnes et al., 2019). Furthermore, residues such as Y10 and E11 are attenuated significantly more than residues C-terminal to these sites (Fig. 6D). It is clear from the ratios of peak intensities with τ values of 200 ms and 5.5 s (Fig. 6D) that the N-terminus of $A\beta_{40}$ remains highly disordered and dynamic in the oligomeric state, while residues Y10-V40 become significantly more ordered and tumble slower than in the monomeric state where the signals would all have decayed to below the detection threshold after a 5.5 s low-pressure period. This result bares similarity with what has been observed for $A\beta_{40}$ fibril structures solved by solid-state NMR (Bertini et al., 2011; Paravastu et al., 2008; Petkova et al., 2002); in all of these fibril structures the N-terminus is unstructured, while the C-terminal residues are the ones that become ordered and are involved in hydrogen bonding. Although some cryo-electron microscopy (cryoEM) structures also found the N-terminus of Aβ40 fibrils to be unstructured (Sachse et al., 2008), other more recent structures showed the N-terminus to be well-ordered and structured in the fibrillar state (Frieg et al., 2024; Yang et al., 2023). Therefore, while the relaxation data point to similarities in terms of secondary structure for the oligomeric and fibrillar states, large differences may also be present.

By lengthening the low-pressure delay, τ, to 8 s (Fig. 6C) and taking the ratio of peak intensities observed at $\tau = 5.5$ and 8 s, the ^{15}N T_1 relaxation times of the oligomeric state can be extracted (Fig. 6E), assuming that the

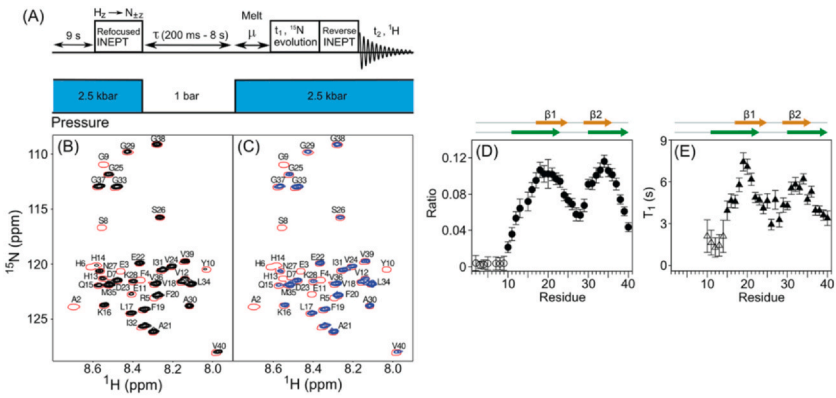

Fig. 6 Measurement of $A\beta_{40}$ ^{15}N T_1 relaxation in the oligomeric state. (A) Schematic representation of the pulse sequence described in detail in Fig. 5. (B) Overlayed HSQC spectra with τ delays of 200 ms (red outline) and 5.5 s (black contours). (C) Overlayed HSQC spectra with τ delays of 200 ms (red outline) and 8 s (blue contours). (D) Intensity ratios between the 5.5-s and 200-ms τ delay spectra. Open circles correspond to the upper limit of the ratio based on signal-to-noise for residues that are not observed when τ is set to 5.5 s (E) Oligomeric ^{15}N T_1 relaxation times determined from the peak ratios when τ is set to 5.5 and 8 s. Open triangles correspond to an upper limit of the ^{15}N T_1 relaxation time for residues that are observed when τ is 5.5 s, but not when τ is 8 s. The position of β-strands, denoted by arrows above panels (D) and (E), correspond to a structure of monomeric $A\beta_{40}$ bound to an affibody by Hoyer et al. (Hoyer et al., 2008) (orange) and from a fibril structure solved by Paravastu et al. (Paravastu et al., 2008) (green). *Adapted with permission from Barnes, C. A., Robertson, A. J., Louis, J. M., Anfinrud, P., & Bax, A. (2019). Observation of β-amyloid peptide oligomerization by pressure-jump NMR spectroscopy. Journal of the American Chemical Society, 141(35), 13762–13766. https://doi.org/10.1021/jacs.9b06970.*

signal decay is monoexponential. After 5.5 s the monomer signals have attenuated more than 4000-fold and are thus undetectable. Therefore, the reported ^{15}N T_1 values are solely from the oligomeric species and do not have any contribution from the monomer. Although residues 10–14 were visible after a low-pressure period of 5.5 s, they were no longer detected after 8 s. They therefore have relatively short ^{15}N T_1's on the order of a few seconds. Residues 15–40 all remain visible after an 8-s low-pressure period and thus have very long ^{15}N T_1 relaxation times. Interestingly, two maxima are observed in the ^{15}N T_1 profile, spanning residues 18–21 and 31–34. The elevated T_1's for these residues indicate that they are highly ordered and therefore likely have β-sheet secondary structure. These regions approximately match the regions that were observed to be β-sheet in the affibody-bound $A\beta_{40}$ structure solved by Hoyer et al. (Hoyer et al., 2008). This

structure was for monomeric $A\beta_{40}$ peptide and had intramolecular hydrogen bonds for residue pairs V18-M35, F20-G33, and E22-I31. The authors proposed that this structure may be the same as the monomeric unit that makes up $A\beta_{40}$ oligomers. This hydrogen bonding contrasts to what is observed for $A\beta_{40}$ fibrils, which have a characteristic parallel in-register cross-β structure in which all of the hydrogen bonds are intermolecular and form β-sheets along the fibril axis (Paravastu et al., 2008). Whether the residues with elevated T_1's are part of an intra- or intermolecular β-sheet and what its registry is cannot be determined by the oligomeric ^{15}N T_1 values alone.

Although the profiles for the magnetization recovered after a 5.5 s low-pressure period and the ^{15}N T_1's are similar, they are not identical. G37 had approximately twice as much magnetization remaining after 5.5 s compared to V40, while they both had T_1's of 3.5–4 s. This indicates that although G37 and V40 reach a comparable degree of structural order after 5.5 s, G37 becomes well-ordered earlier than V40 and loses less magnetization due to T_1 relaxation in a partially disordered state. Thus, residues such as V40 only become fully ordered once the oligomers have grown substantially.

4.3 The effect of Zn^{2+} on oligomeric $A\beta_{40}$ ^{15}N T_1 relaxation

Zn^{2+} is important for neurotransmission and is present at relatively high concentrations in synaptic vesicles and in the synaptic cleft. During synaptic activity, Zn^{2+} can transiently reach micromolar concentrations in the synaptic cleft (Rachline et al., 2005). Elevated levels of Zn^{2+} are also found in the extracellular Aβ plaques in the brains of patients with Alzheimer's disease (Miller et al., 2006). Moreover, Zn^{2+} has been implicated in the formation of cytotoxic $A\beta_{40}$ oligomeric species that are rich in β-sheet content (Solomonov et al., 2012). The three histidines (H6, H13, and H14) in the N-terminal portion of $A\beta_{40}$ coordinate with Zn^{2+} ions (Danielsson et al., 2007), resulting in bridging between monomers and thus the formation of oligomers (Minicozzi et al., 2008). By stabilizing oligomeric assemblies, Zn^{2+} diverts $A\beta_{40}$ from the fibril formation pathway to the production of toxic oligomers.

Zn^{2+} dramatically increases the rate of $A\beta_{40}$ oligomerization (Shen et al., 2022), yet retards the elongation of mature amyloid fibrils (Abelein et al., 2015). These effects, in addition to its biological relevance in $A\beta_{40}$ toxicity, make Zn^{2+} an attractive additive for pressure-jump NMR experiments on oligomeric $A\beta_{40}$. Lower concentrations of $A\beta_{40}$ peptide and higher pH conditions can be used when Zn^{2+} is added to the sample due the accelerated oligomerization. All experiments on $A\beta_{40}$ in the presence of

Zn^{2+} were collected at 293 K in 50 mM sodium phosphite buffer with 5 mM NaCl. The same pulse sequence (Fig. 5 and 6A) used to measure ^{15}N T_1 values of Zn^{2+}-free $A\beta_{40}$ oligomers was applied here, with modifications to the low-pressure delays (τ), spectral widths, and acquisition times. These interleaved ^{15}N T_1 measurements utilized low pressure, τ, delays of 5.5 s and 10 s. The initial τ duration of 5.5 s is sufficient to fully suppress monomer signals, ensuring that the measured relaxation times report exclusively on peptides that oligomerize at rates comparable to or faster than the monomeric ^{15}N R_1 relaxation rate. The 2D HSQC readout spectra for these ^{15}N T_1 measurements were collected with a 15.1-ppm spectral width and 132-ms acquisition time in the direct ^1H dimension, while a 24-ppm spectral width and 68.5-ms acquisition time were used in the indirect ^{15}N dimension. Eight scans were collected per FID, leading to 3200 total pressure cycles for the combined interleaved ^{15}N T_1 experiments. Each full data set required approximately 15 h of acquisition time.

We first sought to test how the concentration of Zn^{2+} affects the oligomeric $A\beta_{40}$ ^{15}N T_1's while keeping the pH and concentration of peptide constant at 7.0 and 500 μM, respectively (Fig. 7A-C). All pH values reported in this chapter are the pH at atmospheric pressure, which in this

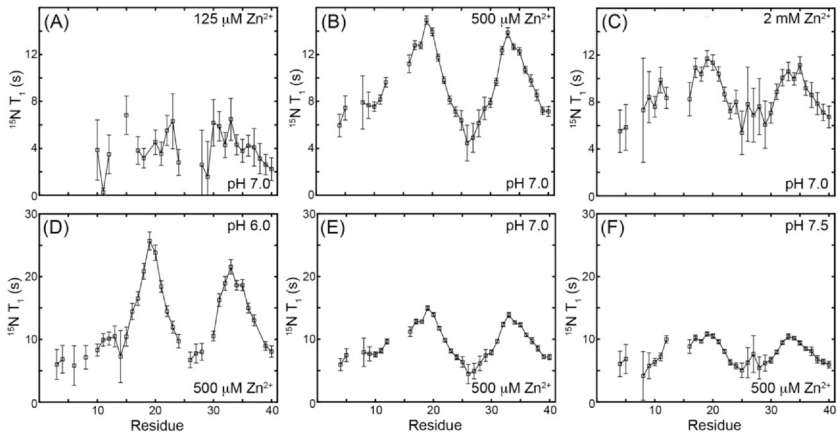

Fig. 7 Zn^{2+} concentration and pH dependence of oligomeric $A\beta_{40}$ ^{15}N T_1 relaxation times. All samples contained 500 μM ^{15}N-labeled $A\beta_{40}$ in 50-mM sodium phosphite buffer with 5 mM NaCl. Experiments were run at 293 K on a 600-MHz spectrometer. A-C) Oligomeric $A\beta_{40}$ ^{15}N T_1 relaxation times in the presence of A) 125 μM Zn^{2+}, B) 500 μM Zn^{2+}, C) 2 mM Zn^{2+}, while keeping the pH constant at 7.0. D-F) Oligomeric $A\beta_{40}$ ^{15}N T_1 relaxation times at D) pH 6.0, E) pH 7.0, F) pH 7.5 while keeping the Zn^{2+} concentration constant at 500 μM. Note (B) and (E) display identical data, but the vertical scales are different to ease the comparison with differing conditions on either side.

case was verified by the phosphite's large scalar J_{PH} coupling (Eykyn & Kuchel, 2003). Note that for both phosphate and phosphite buffers, the pH goes down as the hydrostatic pressure is increased (Caro & Wand, 2018). At a Zn^{2+}:$A\beta_{40}$ stoichiometry of 1:4 (125 μM Zn^{2+}) similar oligomeric ^{15}N T_1 values (Fig. 7A), on the order of 4–6 s for most residues, were observed compared to when the experiment was conducted on 1.3 mM $A\beta_{40}$ at pH 6.0 without Zn^{2+} (Fig. 6E), indicating comparable degrees of structural order and restricted internal mobility. These T_1 values (Fig. 7A) had relatively large errors because only a small fraction of the peptide oligomerized and survived the initial 5.5 s low-pressure delay, τ, likely due to the low stoichiometric ratio of Zn^{2+}:$A\beta_{40}$ and the lower peptide concentration compared to experiments run in the absence of Zn^{2+}. When equimolar amounts of Zn^{2+} and $A\beta_{40}$ were used, significantly longer oligomeric ^{15}N T_1's were obtained (Fig. 7B), with some residues having T_1 relaxation times as long as 14 s. The two regions of the peptide with the longest oligomeric T_1 values remained in the same location compared to when these experiments were run without Zn^{2+}, spanning residues 18–21 and 31–34, but the peaks in the T_1 profile became sharper and more pronounced. Surprisingly, ^{15}N T_1 values of 6 s or more were observed for residues near the N-terminus of $A\beta_{40}$, reaching all the way to F4. These N-terminal residues were found to be dynamically disordered without Zn^{2+}, suggesting that the interaction of Zn^{2+} with the three histidines in the N-terminal half of $A\beta_{40}$, H6, H13, and H14, leads to these residues becoming well-ordered with little internal motion in the oligomeric state. Note that at pH 7.0, exchange processes, including rapid hydrogen exchange with solvent water, broaden the resonances for histidines and their neighboring residues below the detection limit (Geierstanger et al., 1998). Raising the amount of Zn^{2+} in the sample to 2 mM, corresponding to a 4:1 stoichiometric ratio of Zn^{2+}:$A\beta_{40}$, resulted in slightly shorter T_1 values for the well-ordered residues, 18–21 and 31–34, but overall similar T_1 relaxation times for the other residues. We speculate that the excess of Zn^{2+} led to more rapid formation of amorphous or heterogeneous oligomers with a destabilized core, which would have shorter T_1 relaxation times for residues 18–21 and 31–34 than their more ordered counterparts.

A 1:1 stoichiometric ratio of Zn^{2+}:$A\beta_{40}$ produced the longest oligomeric ^{15}N T_1 values, suggesting that equimolar amounts of Zn^{2+} and $A\beta_{40}$ led to the formation of the most well-ordered oligomers. We next tested how varying the pH, while keeping an equimolar stoichiometry of Zn^{2+} and $A\beta_{40}$, affects the oligomeric ^{15}N T_1 relaxation times. Raising the pH from 7.0 to 7.5

resulted in both the maxima and minimum of the oligomeric ^{15}N T_1 profile being slightly broadened; the longest T_1's decreased while the shortest T_1's increased modestly (Fig. 7F). This could suggest that at higher pH values the oligomers become somewhat more heterogeneous or disordered, but that the loop regions have decreased internal mobility. When the pH was dropped to 6.0, the differences in the maxima and minimum of the T_1 profile became more dramatic, with some residues having T_1 values of over 20 s (Fig. 7D), showing that under these sample conditions the oligomers become even more ordered with less internal motions, particularly for the regions that are presumed to be β-sheet. It is perhaps surprising that the oligomers become more ordered at pH 6.0 than pH 7.0 or 7.5, as the histidine sidechain is expected to better chelate Zn^{2+} at pH 7.0 and 7.5, where a greater proportion of its sidechain is neutral, rather than in the positively charged state.

5. Measurement of oligomeric $A\beta_{40}$ ^{15}N T_2 relaxation

5.1 Pulse sequence

The pulse sequence for measuring ^{15}N T_2 relaxation times in the oligomeric state is built off the pulse sequence used to measure ^{15}N T_1 relaxation times in the oligomeric state (Fig. 5). It begins with a refocused INEPT at high pressure to generate in-phase $N_{\pm Z}$ magnetization for the monomeric population of $A\beta_{40}$. The pressure is then dropped to atmospheric pressure for five seconds to allow the $A\beta_{40}$ to oligomerize. This low-pressure delay also serves as a T_1 filter. Since monomeric $A\beta_{40}$ has a ^{15}N T_1 of ~600 ms, while oligomeric $A\beta_{40}$ has T_1's of multiple seconds for many residues, all of the monomeric signal decays during the low-pressure period and only signals from molecules that reached the oligomeric state on a time scale that is fast relative to the monomer ^{15}N T_1 remain. After a delay, T_H, a short Hahn echo interval (Hahn, 1950) with a variable total echo time of τ is included on the ^{15}N channel. ^1H decoupling pulses are applied during the ^{15}N Hahn echo. Similar to the T_1 relaxation experiment, proton inversion pulses are placed during the low-pressure period to mitigate cross-correlation effects arising from the remaining monomer signal, which has a long ^{15}N TROSY T_1 component. These hard inversion pulses are paired with soft inversion pulses centered on the water resonance to keep water magnetization along +z. After the low-pressure period, the pressure is jumped back up to high pressure for a "melting" period of 350 ms. Following the melting period, a reverse INEPT transfers ^{15}N magnetization back to ^1H for detection.

For $A\beta_{40}$, the profile of the detected ^{1}H signals remained virtually unchanged when τ was varied (Fig. 9). In other words, the oligomeric resonances that survive the T_1 filter have uniform T_2 relaxation times. For this reason, combined with the low sensitivity of the experiment and the buildup of pressure-resistant fibrils after a number of pressure cycles, the ^{15}N T_2 relaxation experiment was run as a 1D experiment, rather than by recording a 2D HSQC read-out as was done for the T_1 relaxation experiment. Running this experiment in the 1D mode also enabled the use of three decay times, rather than a two-point measurement as was done for the T_1 relaxation experiment. Three T_H delays, 1.25 s, 2.5 s, and 3.75 s, were used to probe the ^{15}N T_2's as a function of time after the pressure drop. For each of these three T_H delays, three different Hahn echo delays, τ, were used. When $T_H = 1.25$ s, $\tau = 0.02$ ms, 2.5 ms, and 5.0 ms; when $T_H = 2.5$ s, $\tau = 0.02$ ms, 1.0 ms, and 2.0 ms; when $T_H = 3.75$ s, $\tau = 0.02$ ms, 0.5 ms, and 1.0 ms. To minimize the effect that the buildup of pressure-resistant fibrils and decay of free monomer may have on the T_2 decays of the signals, these experiments were run in an interleaved fashion where all three τ values were measured for $T_H = 1.25$, 2.5, 3.75, 3.75, 2.5, 1.25 s. Spectra with the same values of T_H and τ were then co-added for analysis. ^{15}N T_2 relaxation times were determined by extracting the slope after taking the natural logarithm of the relative signal intensity and plotting these values against the three values of τ used. Even though only three τ periods were sampled at each T_H value, each of the decays shows some deviation from exponential decay, indicative of a heterogeneity in size of the oligomers that is present at any given T_H value. For the T_2 experiments a total of 1152 pressure cycles were run, after which the monomer signal had decayed by about 15 %.

5.2 Interpretation of oligomeric $A\beta_{40}$ ^{15}N T_2 relaxation

The decay of the amide signals with various echo delay times, τ, (Fig. 8, Fig. 9A) was uniform across the entire spectrum (Fig. 9B-D) indicating that all residues that survive the 5-s T_1 filter share a common ^{15}N T_2 relaxation time. This suggests that exchange broadening does not play a significant role in the apparent ^{15}N T_2 and that the measured T_2 values are dominated by the J(0) term of the spectral density, meaning that T_2 is inversely proportional to $S^2\tau_c$. S^2 is the generalized Lipari-Szabo order parameter (Lipari & Szabo, 1982), where a value of 0 applies for a protein that is fully disordered, while a value of 1 indicates that the protein is fully rigid. τ_c is the rotational correlation time and is directly proportional to the molecular

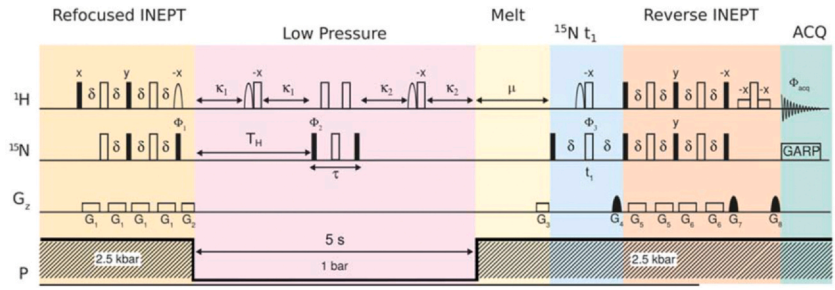

Fig. 8 Pulse sequence for measuring ^{15}N T_2 relaxation times in the oligomeric state (Barnes et al., 2019). Filled and open rectangles on the ^{1}H and ^{15}N radiofrequency channels represent hard 90° and 180° pulses, respectively. Aside from the first shaped pulse at the end of the refocused INEPT, which is a 90° pulse, the shaped pulses denote selective inversion pulses applied to the water resonance, as are the weak rectangular 90° pulses that are part of the standard WATERGATE (Piotto et al., 1992) element. Unless otherwise stated, all pulses are applied along x. This pulse sequence is essentially identical to that used for measuring the ^{15}N T_1 relaxation times (Fig. 5) except for the inclusion of a ^{15}N Hahn echo (Hahn, 1950) during the low-pressure oligomerization delay, and that the experiment was run in an interleaved 1D fashion, with $t_1 = 0$. Delays κ_1 and κ_2 are varied such that the 180°(water)–180° pulse pairs are centered within their respective delay intervals as the Hahn-echo block is moved across the 5-s T_1 filter. Pulsed field gradients are either sine-bell shaped ($G_{4,\ 7,\ 8}$), or weak rectangular ($G_{1,\ 2,\ 3,\ 5,\ 6}$). Phase cycling: $\varphi_1 = \{y, -y\}$, $\varphi_2 = \{x, x, -x, -x\}$, $\varphi_3 = \{x, x, x, x, y, y, y, y, -x, -x, -x, -x, -y, -y, -y, -y\}$, $\varphi_{acq} = \{x, -x, -x, x, -x, x, x, -x\}$. Gradient durations and peak amplitudes are as follows: G_1, 2.6 ms, 1.8 %; G_2, 2.0 ms, 15.6 %; G_3, 1.0 ms, 6.2 %; G_4, 2.0 ms, 29.6 %; G_5, 2.6 ms, 0.7 %; G_6, 2.6 ms, 0.5 %; G_7, 0.5 ms, 18.0 %; G_8, 0.5 ms, 30 %, where 100 % corresponds to a gradient strength of 53 G/cm. *Reprinted with permission from Barnes, C. A., Robertson, A. J., Louis, J. M., Anfinrud, P., & Bax, A. (2019). Observation of β-amyloid peptide oligomerization by pressure-jump NMR spectroscopy. Journal of the American Chemical Society, 141(35), 13762–13766. https://doi.org/10.1021/jacs.9b06970.*

weight of the species being probed. Only rigid, well-ordered residues survive the 5-s low-pressure T_1 filter, therefore S^2 must be high (>∼0.7) for magnetization to remain observable after a 5-s low-pressure interval. ^{15}N T_2 measurements are therefore a good proxy for studying the growth of $A\beta_{40}$ oligomers after a pressure drop.

When T_H was set to 1.25 s (Fig. 9B,E), the ^{15}N T_2 was ∼3.7 ms, which is nearly two orders of magnitude shorter than for the intrinsically disordered monomer, showing that after only 1.25 s the oligomers have grown to a considerable size. Assuming isotropic tumbling and an order parameter, S^2, of 0.85, a 3.7-ms ^{15}N T_2 corresponds to a rotational correlation time, τ_c, of about 200 ns. A ∼350 kDa oligomer, or an ∼80-mer of

$A\beta_{40}$, would have a rotational correlation time of ~200 ns. When T_H is increased to 2.5 s (Fig. 9C,E), the ^{15}N T_2 decreases to ~1.7 ms, which would correspond to a ~750 kDa oligomer, or a 170-mer. The ^{15}N T_2 further decreased to 1.0 ms when the T_2 was probed 3.75 s after the pressure drop (Fig. 9D,E), corresponding to a ~1.3 MDa oligomer or a 300-mer. These results demonstrate that $A\beta_{40}$ oligomers, formed following a pressure drop, grow rapidly to hundreds of monomer units within seconds and continue to increase in size throughout the timescale that was probed in these T_2 measurements.

The ^{15}N T_2 decay (Fig. 9E) is not fully exponential; if it were, each of the points in Fig. 9E would fall precisely on the linear fit in a semi-log plot.

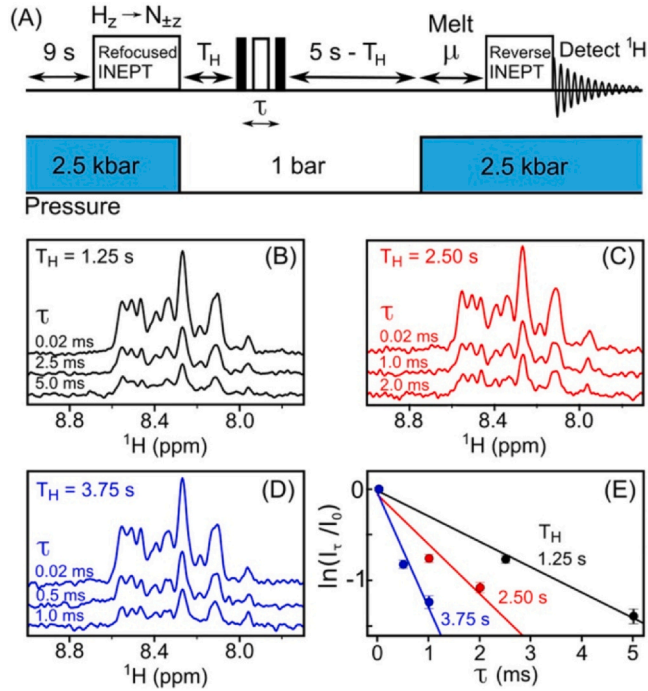

Fig. 9 Measurement of $A\beta_{40}$ ^{15}N T_2 relaxation in the oligomeric state. (A) Schematic representation of the pulse sequence described in detail in Fig. 7. (B-D) 1D proton amide signals after various Hahn-echo delays, τ, for (B) $T_H = 1.25$ s, (C) $T_H = 2.5$ s, and (D) $T_H = 3.75$ s (E) Intensity decays as a function of τ are shown on a logarithmic scale for the three values of T_H. *Reprinted with permission from Barnes, C. A., Robertson, A. J., Louis, J. M., Anfinrud, P., & Bax, A. (2019). Observation of β-amyloid peptide oligomerization by pressure-jump NMR spectroscopy. Journal of the American Chemical Society, 141(35), 13762–13766. https://doi.org/10.1021/jacs.9b06970.*

However, for all three T_H times, the second time point falls slightly below the linear fit. In other words, the relaxation is faster at short values of τ and slower at longer values of τ. This indicates that there is heterogeneity in the size of the oligomers, with the measured T_2 values reflecting the approximate average size of oligomers at each T_H time point.

6. Amelotin: A model oligomeric protein for developing pressure-jump NMR experiments

6.1 Amelotin forms oligomers that can be dissociated with pressure

Amelotin is a protein involved in hydroxyapatite mineralization during enamel formation (Fouillen et al., 2017). Mice with the amelotin gene knocked out exhibit hypomineralized enamel (Abbarin et al., 2015). Full-length amelotin, comprised of 201 residues, at a concentration of 5 μM yields a ^{1}H-^{15}N HSQC spectrum indicative of an intrinsically disordered protein (IDP); all the expected resonances are visible, with sharp linewidths and near-random-coil chemical shifts (Chiliveri et al., 2023). However, many of the resonances broaden out below the detection limit when the concentration is raised to 500 μM, indicating that the protein has oligomerized and these regions are tumbling too slowly to be visible in a solution NMR spectrum (Ren et al., 2021). Dynamic light scattering (DLS) revealed roughly spherical, polydisperse oligomers with diameters of 10–30 nm. The fact that some residues remain visible in an HSQC spectrum at elevated concentrations indicates that only part of the protein becomes structured in the oligomeric state, while other parts remain highly dynamically disordered. At a pressure of 2 kbar, 500 μM amelotin fully dissociates into its monomeric IDP state, and all of its expected resonances become visible in an HSQC spectrum.

A truncated construct of amelotin comprised of residues 25–130, encompassing all residues identified as part of the oligomerization domains in the full-length protein, exhibits the same pressure-dependent behavior as the full-length construct. Furthermore, the chemical shifts of this truncated construct at high pressure match with those of the full-length protein, thus providing evidence that the two constructs behave similarly in solution. With diameters ranging from about 8–20 nm, DLS measurements of the truncated construct showed the average size of its oligomers to be slightly smaller than those of the full-length protein. Below, we describe experiments developed

on this truncated amelotin construct, with the aim to apply them to $A\beta_{40}$ which is much harder to express in the required quantities and rapidly forms pressure-resistant fibrils, limiting the number of pressure cycles that can be employed in any given experiment. All experiments were carried out on a 900 MHz spectrometer using 500 μM $^{2}H,^{13}C,^{15}N$-labeled amelotin$^{25–130}$ in 30 mM sodium acetate buffer (pH 4.6) with 70 mM NaCl at 288 K.

Amelotin rapidly forms oligomers at atmospheric pressure (Ren et al., 2021) and rapidly dissociates into its intrinsically disordered monomeric state at high pressure (Chiliveri et al., 2023). It can undergo well over 100,000 pressure cycles before the onset of pressure-resistant aggregate formation. The ability to execute tens of thousands of pressure cycles with minimal signal loss makes amelotin a great model system for developing new pressure-jump NMR experiments to study proteins in their oligomeric state. Once developed and proven useful, they then can then be applied to systems that are more challenging in terms of sample preparation, such as $A\beta_{40}$, by employing very sparse non-uniform sampling (NUS) (Barna et al., 1987; Orekhov et al., 2011; Rovnyak et al., 2004) to minimize the number of pressure cycles needed to extract useful high-resolution structural information.

6.2 Measurement of secondary shifts in the oligomeric state

Regions of the amelotin protein that form the structured oligomeric species are NMR-invisible at atmospheric pressure due to their slow molecular tumbling and its associated fast transverse relaxation. While these residues become visible in a ^{1}H-^{15}N HSQC at 2 kbar, information on the structure of the oligomeric species is lost as the entire protein becomes intrinsically disordered and simply adopts random coil chemical shifts for all residues. A pseudo-3D stroboscopic chemical shift measurement (Charlier et al., 2018b; Chiliveri et al., 2023) (Fig. 10A) can be utilized to probe the population weighted average chemical shifts of the NMR-invisible species with a high-pressure and thus high-sensitivity HSQC readout.

The pseudo-3D stroboscopic chemical shift pulse sequence is built using the same elements as the experiments used to measure ^{15}N T_1 and T_2 relaxation times for oligomeric $A\beta_{40}$ (Barnes et al., 2019). One key difference for designing experiments for amelotin is that the oligomers formed by amelotin are smaller and not as well ordered as those observed for $A\beta_{40}$. While $A\beta_{40}$ had ^{15}N T_1 relaxation times on the order of 3–6 s for its ordered regions, amelotin has T_1 relaxation times of 1.4–2 s for its ordered regions; therefore, a long ^{15}N T_1 filter cannot be utilized to filter out all of

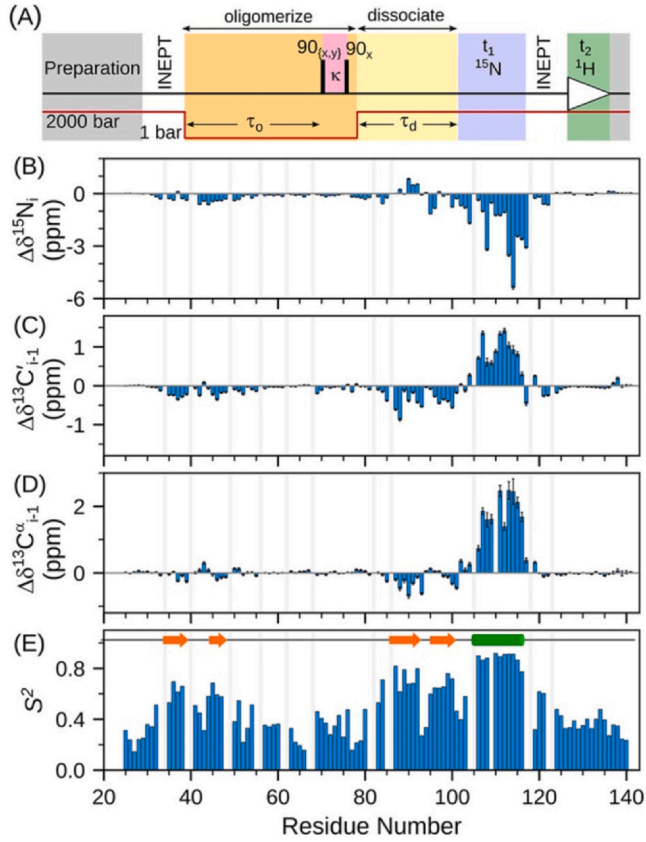

Fig. 10 Oligomeric amelotin secondary chemical shifts. (A) Schematic representation of the pseudo-3D stroboscopic chemical shift measurements (Charlier et al., 2018b; Chiliveri et al., 2023) used to measure chemical shifts in the oligomeric state. All INEPT transfers were done at 2 kbar where amelotin is a monomeric IDP with long T_2 relaxation times. Following the initial INEPT transfers, the pressure was dropped to atmospheric pressure and the protein was allowed to oligomerize for a time, τ_o. At the end of τ_o, secondary shifts were encoded stroboscopically. A melting period, τ_d, is then included where the sample is brought up to 2 kbar to dissociate the oligomers, followed by a ^{1}H-^{15}N HSQC readout. (B-D) Secondary shifts for ^{15}N, ^{13}C′, and ^{13}C$^\alpha$, respectively. (E) Generalized order parameters, derived from the Random Coil Index (Berjanskii & Wishart, 2005), predicted from the secondary shifts using TALOS-N (Shen & Bax, 2015). Regions predicted to be β-sheet are marked by orange arrows, while the region with α-helical chemical shifts is marked by a green cylinder. *Reprinted with permission from Chiliveri, S. C., Shen, Y., Baber, J. L., Ying, J., Sagar, V., Wistow, G., Anfinrud, P., & Bax, A. (2023). Experimental NOE, chemical shift, and proline isomerization data provide detailed insights into amelotin oligomerization. Journal of the American Chemical Society, 145(32), 18063–18074. https://doi.org/10.1021/jacs.3c05710.*

the remaining monomer signal when studying the oligomer. To measure ^{15}N secondary shifts, the pulse sequence is almost identical to the one used to measure ^{15}N T_2 relaxation times (Fig. 8). It begins with a refocused INEPT at high pressure to generate $N_{\pm z}$ magnetization, followed by a pressure drop to allow the protein to oligomerize for a time, τ_o, which was chosen to be 299 ms for amelotin experiments. The only difference is that instead of a Hahn echo on the ^{15}N channel, the 180° pulse is omitted so that a single, short chemical shift evolution time is measured. Depending on the phase of the first 90° pulse preceding this short chemical shift evolution, either the cosine- or sine-modulated component is read out. The ^{15}N chemical shift is then given by $\omega = \kappa^{-1}\tan^{-1}(I_x/I_y)$, where κ is the chemical shift evolution delay (0.55 ms in this case); I_x and I_y correspond to the signal intensities when the first 90° pulse has a phase of x or y, respectively, which are the cosine- and sine-modulated components, respectively. After the short chemical shift evolution, the pressure is jumped back up to 2 kbar for τ_d = 300 ms to dissociate the oligomers, followed by a high sensitivity HSQC readout (Kay et al., 1992).

In addition to the obvious time-saving benefit of only requiring two points to measure the population weighted average chemical shift (Hansen & Brüschweiler, 2016; Kupče & Freeman, 2007), as opposed to measuring a full chemical shift dimension, the stroboscopic chemical shift measurement can determine the chemical shifts even when the T_2 relaxation is very fast. For amelotin, the ^{15}N T_2 relaxation times are on the order of 3 ms for the well-ordered oligomeric regions (Chiliveri et al., 2023); therefore, losses due to T_2 relaxation during the 0.55 ms ^{15}N chemical shift evolution period are less than ~20 %.

Besides secondary structure, ^{15}N secondary shifts are impacted substantially by a wide range of other structural features (de Dios et al., 1993). Combining them with other backbone secondary shifts, including ^{13}C' and $^{13}C^{\alpha}$, allows the use of software, such as TALOS-N (Shen & Bax, 2015), to predict the secondary structure and the generalized order parameter, S^2 (Berjanskii & Wishart, 2005), at residue-specific resolution. The pulse sequences to measure ^{13}C' and $^{13}C^{\alpha}$ secondary shifts are very similar to the pulse sequence used to measure ^{15}N secondary shifts. The key difference is that instead of a single refocused INEPT at the beginning of the experiment that generates in-phase $N_{z,i}$ magnetization, to measure ^{13}C' chemical shifts two INEPT steps are needed to generate $N_{z,i}C'_{z,i-1}$ magnetization; to measure $^{13}C^{\alpha}$ secondary shifts three INEPT transfers are required to generate $N_{z,i}C'_{z,i-1}C^{\alpha}_{z,i-1}$ magnetization. Just as the $^{15}N_i$ chemical shift is

stroboscopically probed after τ_o, the $^{13}C'_{i-1}$ and $^{13}C^{\alpha}_{i-1}$ chemical shifts are stroboscopically encoded after τ_o, before the pressure is jumped back up to 2 kbar to dissociate the oligomers for τ_d, followed by reverse INEPT steps and HSQC readout elements. Note that the ^{15}N stroboscopic measurements detect the chemical shift of residue i, while the $^{13}C'$ and $^{13}C^{\alpha}$ measurements observe the chemical shift of residue i-1. κ values of 0.35 ms were used for measuring $^{13}C'$ and $^{13}C^{\alpha}$ secondary shifts while τ_o and τ_d remained at 299 and 300 ms, respectively. Measurement of $^{13}C'$ and $^{13}C^{\alpha}$ chemical shifts requires that the lifetime of the C'_z spin state be long relative to the INEPT transfer delay of ~30 ms. For very slowly tumbling oligomers, such as those observed for $A\beta_{40}$, this can become a limiting factor due to efficient $^{13}C'$-$^{13}C^{\alpha}$ spin flips.

For amelotin residues Q106-L116, ^{15}N, $^{13}C'$, and $^{13}C^{\alpha}$ all show secondary shifts in the oligomeric state that are characteristic of α-helical structure (Wishart & Sykes, 1994) (Fig. 10B-D). Additionally, there are four short stretches that TALOS-N identifies as β-sheet, spanning residues 34–39, 45–48, 87–93, and 95–101 (Fig. 10E). The β-sheet secondary shifts are relatively small compared to the α-helical shifts, suggesting that these regions retain significant internal flexibility. This interpretation is supported by the relatively low random-coil-index derived generalized order parameter, S^2 (Berjanskii & Wishart, 2005), predicted for these regions, which is smaller than what is typically observed for globular proteins. An alternative explanation for the relatively small secondary shifts and S^2 values is that the stroboscopic chemical shift measurements are reporting the population-weighted average chemical shifts of two populations: the intrinsically disordered monomer and a rigid, well-ordered oligomeric population. Signals arising from the intrinsically disordered monomer cannot be fully separated from the oligomeric species in these experiments because they have T_1 values that differ by only a factor of ~2. Because the τ_o was set to 300 ms, a regime in which neither the monomeric nor oligomeric species has largely decayed before stroboscopically encoding the chemical shifts, the admixture of both states is measured. However, considering that the chemical shifts for the helical region appear close to fully developed, and that the rate at which the secondary chemical shifts develop after the pressure drop is similar across the entire sequence, the smaller secondary chemical shifts outside the helical region are likely resulting from large amplitude internal dynamic processes.

These experiments to stroboscopically measure the secondary shifts in the oligomeric state of amelotin can, at least in principle, be applied directly

to $^{2}H,^{13}C,^{15}N$-labeled $A\beta_{40}$. Measurement of secondary shifts for the $A\beta_{40}$ oligomer would facilitate the confirmation, or disagreement, with the proposed β-sheet secondary structure for residues 18–21 and 31–34 and the dynamic disorder for the N-terminal residues. However, rapid $^{13}C'$ spin-flips resulting from J(0) dipolar ^{13}C-^{13}C interactions make measurement of $^{13}C'$ and $^{13}C^{\alpha}$ chemical shifts for $A\beta_{40}$ more challenging than for amelotin.

6.3 Measurement of NOEs in the oligomeric state

Chemical shifts measured for the oligomeric state of amelotin provide information about its secondary structure. However, chemical shifts do not report on the tertiary or quaternary structure of the oligomer. Distance restraints, such as those derived from nuclear Overhauser Effects (NOEs) (Herrmann et al., 2002), or long-range angular restraints provided by residual dipolar couplings (RDCs) (Chiliveri et al., 2022; Rohl & Baker, 2002), are necessary to start unraveling the three-dimensional structure of the oligomeric species. Due to the short T_2 relaxation times associated with the oligomeric species, measurement of its RDCs is challenging and likely intractable. ^{1}H-^{1}H NOEs, on the other hand, are straightforward to measure as long as the oligomerization occurs on a time scale that is relatively fast compared to the proton T_1. IDPs have very small ^{1}H chemical shift dispersion but have relatively large dispersion in the ^{15}N dimension. Therefore, to gain site-specific resolution for a protein like amelotin in its disordered state, these experiments are best recorded as a 3D ^{15}N-^{15}N-^{1}H HMQC-NOESY-HSQC spectrum in which both of the indirect dimensions are evolved on ^{15}N (Fig. 11A) (Frenkiel et al., 1990; Ikura et al., 1990). This experiment consists of an initial HMQC block followed by a ^{1}H-^{1}H NOESY mixing period and a subsequent HSQC read-out. Because the amelotin sample is perdeuterated, the resulting spectra contain only amide-to-amide ^{1}H-^{1}H NOE contacts, but at considerably improved sensitivity over protonated proteins because magnetization is not diluted by spin diffusion to aliphatic sites (LeMaster, 1989; Torchia et al., 1988).

When the 3D NOESY experiment is recorded at static high-pressure conditions with $T_{NOE} = 150$ ms, only weak NOEs to sequential amides are observed (Fig. 11B), as expected for an IDP where the dynamic disorder leads to slow ^{1}H-^{1}H cross-relaxation. However, introducing a 100 ms low-pressure period, T_{LP}, during the NOESY mixing period produces a markedly different outcome (Fig. 11C). Under these pressure-jump conditions, the slowly tumbling, well-ordered oligomeric species produces

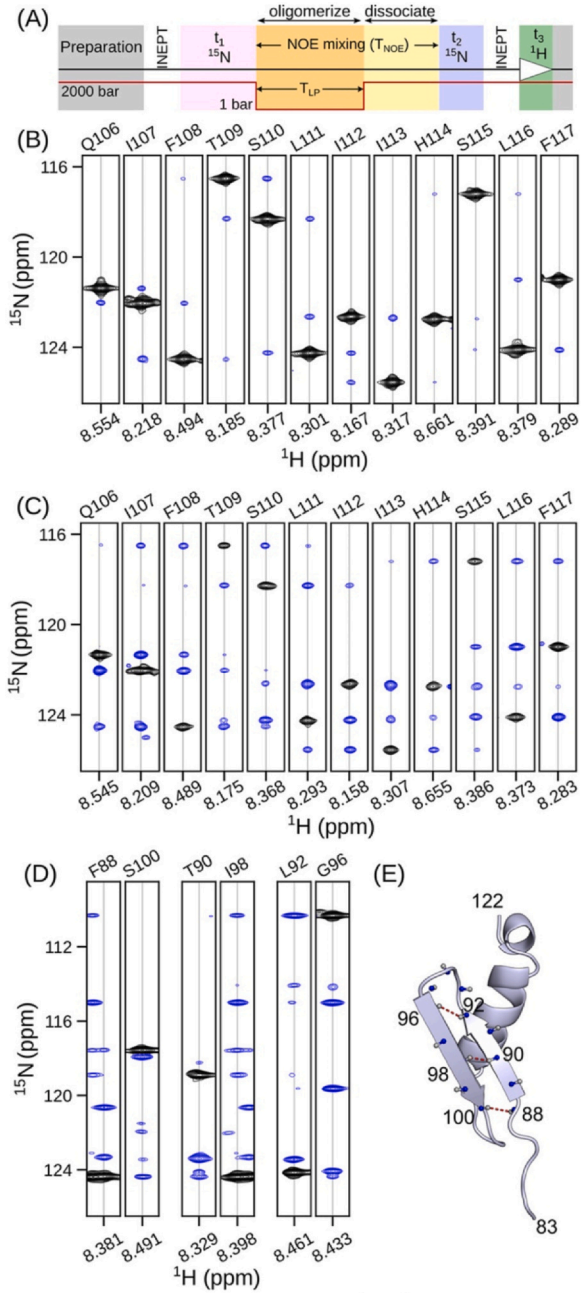

Fig. 11 Measurement of ^{1}H-^{1}H NOEs in oligomeric amelotin. (A) Schematic representation of the 3D ^{15}N-^{15}N-^{1}H HMQC-NOESY-HSQC experiment (Chiliveri et al., 2023; Frenkiel et al., 1990; Ikura et al., 1990). In this experiment all radiofrequency pulses are

numerous strong NOE cross peaks. The α-helical region of amelotin (Q106-L116) exhibits extensive spin diffusion as evidenced by cross peaks extending well past sequential contacts, even reaching as far as three residues away (Fig. 11C).

More interestingly, unambiguous long-range amide-amide NOEs were observed for F88-S100, T90-I98, and L92-G96 (Fig. 11D). These residues were predicted by TALOS-N to be in β-sheets based on their backbone secondary shifts; the NOEs indicate the presence of an antiparallel β-sheet between the β-strands formed by residues 87–93 and 95–101. With a fully isotopically labeled sample it is unclear whether these contacts are intra- or intermolecular in nature. To resolve this ambiguity, the experiment was repeated on a sample containing a 1:1 ratio of $^{2}H,^{13}C,^{15}N$:$^{2}H,^{12}C,^{14}N$-labeled protein. Intramolecular contacts will have the same relative cross peak to diagonal ratio, while intermolecular contacts will have their cross peak to diagonal ratio go down two-fold (Folmer et al., 1995; Lee et al., 1994). All three of the long-range contacts listed above had the same relative cross peak to diagonal ratio using this labeling scheme and are thus part of an intramolecular β-sheet.

Running AlphaFold2 (Jumper et al., 2021) on monomeric amelotin (residues H83-L122) predicted an α-helix for residues E103-S115, which correlates well with the α-helix predicted by TALOS-N using the secondary shifts measured for the oligomeric species. However, AlphaFold2 did not predict the antiparallel β-sheet described above. AlphaFold-

applied at high pressure. The pressure is only briefly dropped to atmospheric pressure during the NOE mixing period to allow the protein to oligomerize. The protein is then dissociated during a "melting" period, included as the second part of the NOE mixing period, prior to the HSQC readout. (B) Strip plots for residues Q106-F117 from a static high-pressure experiment in which the NOE mixing time was set to 150 ms. (C) Strip plots for residues Q106-F117 from a pressure-jump experiment with a low-pressure time of 100 ms at the start of a 150-ms NOE mixing time. (D) Strip plots showing long-range, intramolecular contacts from an antiparallel β-sheet for residue pairs F88-S100, T90-I98, and L92-G96. In (B-E), for clarity, diagonal peaks are shown in black and cross peaks are shown in blue. (E) Monomer portion comprising residues H83-L122 from a structure for hexameric amelotin predicted by one out of many AlphaFold-Multimer models (Evans et al., 2022; Jumper et al., 2021). *Reprinted with permission from Chiliveri, S. C., Shen, Y., Baber, J. L., Ying, J., Sagar, V., Wistow, G., Anfinrud, P., & Bax, A. (2023). Experimental NOE, chemical shift, and proline isomerization data provide detailed insights into amelotin oligomerization. Journal of the American Chemical Society, 145(32), 18063–18074. https://doi.org/10.1021/jacs.3c05710.*

Multimer (Evans et al., 2022) was then used to evaluate whether it could generate plausible oligomeric models. One of the many predicted structures of hexameric amelotin (residues H83-L22) exhibited both the α-helical segment and the intramolecular antiparallel β-sheet with the correct registry (Fig. 11E). Although this monomeric unit from the hexameric structure prediction fits both the secondary structure and intramolecular NOEs that were experimentally determined for amelotin, the hexameric structure is inconsistent with most of the intermolecular NOEs that were determined from the mixed labeled sample, such as L85-V89 and Q91-S100 (Chiliveri et al., 2023). AlphaFold-Multimer therefore predicted a plausible monomer structure, but the quaternary arrangement of these monomers is not consistent with experimental evidence. DLS indicated the average size of oligomers to be much larger than a hexamer, but AlphaFold-Multimer failed to make high confidence predictions for any oligomeric species larger than a hexamer. These results suggest that while AlphaFold provides a plausible local structure for oligomeric amelotin, it does not yet reliably model the higher-order organization of the oligomeric assembly.

Just as the pressure-jump stroboscopic chemical shift experiments on oligomeric amelotin can be directly applied to $A\beta_{40}$, the pressure-jump 3D ^{15}N-^{15}N-^{1}H HMQC-NOESY-HSQC experiment can in principle be applied to deuterated $A\beta_{40}$. However, there exist two significant problems in applying this pressure-jump NOESY experiment to measuring long-range contacts for oligomeric $A\beta_{40}$: the rates at which $A\beta_{40}$ oligomerizes and dissociates are lower than for amelotin, and the rapid buildup of pressure-resistant $A\beta_{40}$ fibrils after a few thousand pressure cycles limits the number of transients that can be collected. Under the conditions used to measure $A\beta_{40}$ ^{15}N T_1 and T_2 relaxation times, it took a second for approximately half of the peptide to oligomerize (Fig. 4C) (Barnes et al., 2019), which is an order of magnitude slower than what is desired to limit the losses due to ^{1}H T_1 relaxation during the NOESY mixing period. Therefore, the rate of oligomerization for $A\beta_{40}$ must be accelerated to build up appreciable NOEs in the oligomeric state. The pressure-jump NOESY experiment on amelotin lasted 42 h and consisted of over 15,000 pressure cycles. Half of the $A\beta_{40}$ monomer had been converted to pressure-resistant fibrils after only 3000 pressure cycles (Fig. 3A). Therefore, a far sparser NUS sampling schedule is required to collect a similar spectrum for $A\beta_{40}$ compared to amelotin.

7. Long-range NOEs in oligomeric $A\beta_{40}$

7.1 Sample optimization for oligomeric NOE measurements on $A\beta_{40}$

While results for amelotin demonstrated that meaningful distances in the oligomeric state can be obtained from 3D pressure-jump NOESY experiments on perdeuterated, amide-protonated protein, the success of this experiment hinges on rapid conversion of the protein between oligomeric and monomeric states. Whereas for amelotin, these rates were $\sim 30\,s^{-1}$ (Chiliveri et al., 2023), re-optimization of $A\beta_{40}$ sample conditions was required to reach rates that were sufficiently fast for such measurements.

The measurement of ^{15}N T_1 and T_2 relaxation times in the oligomeric state of $A\beta_{40}$ required that the kinetics of oligomerization and dissociation were on the order of, or faster than, the ^{15}N T_1 relaxation time. These relaxation times were probed after in phase $N_{\pm z}$ magnetization was generated at high pressure and the pressure was subsequently dropped to atmospheric pressure to allow the monomeric $A\beta_{40}$ to oligomerize. In contrast, ^{1}H-^{1}H NOEs are measured when the magnetization is on protons (Fig. 11A) and in this case the oligomerization and dissociation of oligomers needs to be fast relative to the proton T_1, which limits the maximum NOE mixing time that can be afforded in an experiment (Chiliveri et al., 2023). Under the sample conditions used to measure ^{15}N T_1 and T_2 relaxation times, only about half of the peptide had oligomerized after 1 s (Barnes et al., 2019), while for a NOESY experiment the oligomerization and dissociation would ideally be faster than a few tens of milliseconds to allow for both the oligomerization and dissociation to occur during the ^{1}H-^{1}H NOE mixing period. Therefore, the rate of oligomerization and dissociation desired for a NOESY experiment is over an order of magnitude faster than what was needed to measure the oligomeric T_1 and T_2 relaxation times.

The rate at which $A\beta_{40}$ oligomerizes is a function of pH, peptide concentration, and temperature. Although raising the temperature did indeed accelerate oligomerization, it also strongly increased the rate of pressure resistant fibril formation. Consequently, the temperature was kept at 293 K for all $A\beta_{40}$ NOESY experiments. Oligomerization was found to be fastest at a pH of 4.5 in 50 mM sodium acetate buffer, which was therefore selected as the buffer for NOESY experiments on $A\beta_{40}$. Peptide concentrations of 1.6–2.0 mM were found to be sufficiently high to result in significant oligomerization within 100 ms in this buffer. Importantly, the

dissociation is also rather fast under these solution conditions, such that a 100-ms melting period during the NOE mixing resulted in most of the oligomeric population dissociating into monomers. One third to one half of the peptide was converted to pressure-resistant fibrils after 1600 pressure cycles under these sample conditions, thus limiting the number of FIDs that could be collected in a single experiment to 800 for a pulse sequence with a two-step phase cycle.

$A\beta_{40}$ samples for NOESY experiments were prepared in a similar manner to the samples used for measuring oligomeric ^{15}N relaxation times. Lyophilized peptide was first dissolved in 95 μL of 10 mM sodium hydroxide to fully monomerize the peptide in solution. The pH was then dropped to 4.5 by the addition of 95 μL of a buffer containing 100 mM sodium acetate, 10 mM HCl, and 2 mM EDTA such that the final sample contained 50 mM sodium acetate, pH 4.5, 5 mM NaCl and 1 mM EDTA. All solutions used in this preparation contained 3 % D_2O for the deuterium lock.

Perdeuteration was required for the NOESY experiments in order to prevent the spin diffusion of amide proton magnetization to the vast excess of non-exchangeable protons, which otherwise would result in a severe sensitivity drop. All peptides for NOESY experiments were produced in-house, as perdeuterated $A\beta_{40}$ is not commercially available. Essentially the same expression and purification protocol was used as for the ^{15}N-labeled $A\beta_{40}$ (Barnes et al., 2019; Ying et al., 2019) aside from the use of 99.9 % D_2O and perdeuterated glucose as the sole carbon source in the M9 minimal media. For methyl sidechain to backbone amide NOE experiments, protonated, ^{13}C-labeled methyl groups were introduced for isoleucine, leucine, and valine (ILV) in an otherwise perdeuterated background. ILV labels were incorporated with the use of α-ketobutyrate and α-ketoisovalerate precursors (Tugarinov et al., 2006).

7.2 Measurement of backbone-to-backbone amide NOEs on oligomeric $A\beta_{40}$

The two regions with the most strongly elevated ^{15}N T_1's for oligomeric $A\beta_{40}$, spanning residues V18-A21 and I31-L34 (Fig. 6E), indicate that these two regions are particularly well-ordered in the oligomeric state and presumably are involved in the formation of a β-sheet (Barnes et al., 2019). However, the T_1 values give no information on which residues are hydrogen bonded and what their registry is. Just as backbone-to-backbone amide proton NOEs revealed the location and registry of β-sheets for amelotin (Fig. 11D) (Chiliveri et al., 2023), a 3D pressure-jump ^{15}N-^{15}N-^{1}H

HMQC-NOESY-HSQC experiment can be used to probe which residues are hydrogen bonded in oligomeric $A\beta_{40}$. In an antiparallel β-sheet the amide protons of hydrogen-bonded residues are on average 3.3 Å apart (Hwang et al., 2002), while in a parallel β-sheet the closest amide to amide proton distances between neighboring β-strands is ~3.7 Å (Friedrich et al., 2020). Both distances are short enough that they should produce observable ^{1}H-^{1}H NOEs and help to identify the position and registry of β-sheets from a NOESY experiment.

Both the high-pressure static and pressure-jump ^{15}N-^{15}N-^{1}H HMQC-NOESY-HSQC experiments on $A\beta_{40}$ (Fig. 12A) were recorded with the same pulse sequence that was used to measure NOEs for amelotin (Fig. 11), but with different NOE mixing times. A 200-ms NOE mixing period was used for both experiments, with the pressure-jump experiment including a 100-ms low-pressure delay, T_{LP}, at the start of the NOE mixing. Both experiments were conducted with 100 complex points in both ^{15}N indirect dimensions, using a spectral width of 22 ppm and evolution times of 74.7 ms on a 600-MHz spectrometer. The direct (^{1}H) dimension was acquired for 213 ms. 5 % time-ordered NUS sampling was used for the static experiment, while 2 % time-ordered NUS sampling was used for the pressure-jump experiment (Ying et al., 2019) leading to total experimental times of 2.75 and 4.25 h for the static and pressure-jump experiments, respectively, when their recycle delays of 1.8 and 9 s are taken into consideration.

With a two-step phase cycle, the 2 % NUS sampling for the pressure jump experiment resulted in a total of 800 FIDs being collected, corresponding to 1600 pressure cycles. This very sparse NUS protocol was necessary due to the rapid buildup of pressure-resistant fibrils under the solution conditions used. Despite the sparse sampling, these spectra were of high quality and showed NOE cross peaks being significantly more intense than reconstruction artifacts (Ying et al., 2017).

As expected for an intrinsically disordered peptide, the static high-pressure NOESY experiment yielded intense diagonal peaks with weak sequential cross peaks (Fig. 12A); no medium- or long-range cross peaks were observed in the static experiment. However, a very different spectral pattern was observed when pressure was temporarily switched to low during the first 100 ms of NOE mixing, which allowed the peptide to oligomerize and resulted in NOE contributions from the oligomeric state. The pressure-jump spectrum yielded numerous long-range cross peaks (Fig. 12A). These long-range cross peaks pertained to the same regions of the peptide that had elevated ^{15}N T_1's (Fig. 6E). The sequential cross peaks

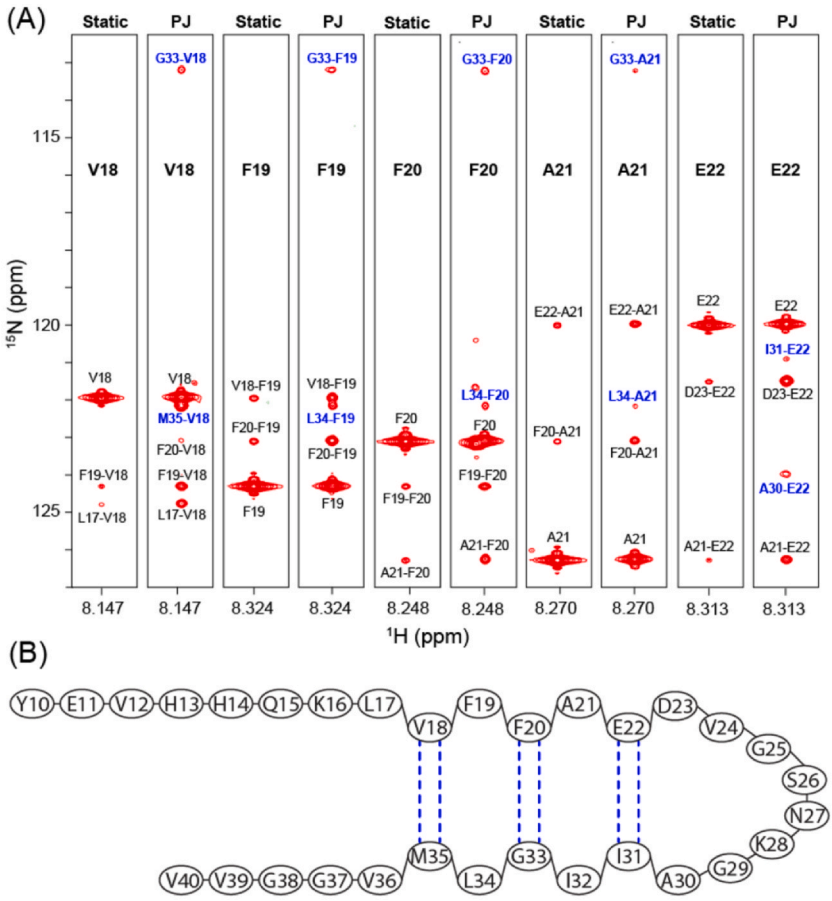

Fig. 12 Backbone-to-backbone amide NOEs for oligomeric $A\beta_{40}$. (A) Strip plots taken from a 3D ^{15}N-^{15}N-^{1}H HMQC-NOESY-HSQC spectrum that was recorded on ^{2}H,^{15}N-labeled $A\beta_{40}$. These experiments were identical to those recorded for amelotin (Fig. 11) aside from different NOE mixing delays. Both the static high-pressure, and pressure-jump experiments were conducted with a 200-ms NOE mixing period, where the pressure-jump experiment included a 100-ms low-pressure period, T_{LP}, at the beginning of NOE mixing to allow the peptide to oligomerize. Long-range cross peaks are labeled with blue text. (B) Schematic representation of the proposed antiparallel, intramolecular β-sheet formed by $A\beta_{40}$ in the oligomeric state. Hydrogen bonds between V18-M35, F20-G33, and E22-I31 are inferred from the long-range cross peaks identified in (A). Residues D1-G9 are omitted from this diagram as they were found to be dynamically disordered based on the ^{15}N T_1 measurements. Data were recorded at 600 MHz in 50 mM sodium acetate, pH 4.5, 5 mM NaCl and 1 mM EDTA at 293 K.

also became relatively much more intense, despite the sequential H^N-H^N distance being rather long (~5 Å) in a β-sheet. This result indicates that NOE transfer efficiencies are greatly enhanced in the oligomeric state compared to the dynamically disordered monomeric state.

Even though the peptide was deuterated, spin diffusion between amide protons was pervasive (Horst et al., 2006) as exemplified by the observation that G33's amide proton showed NOEs to V18, F19, F20, and A21 (Fig. 12A). This extensive spin diffusion made it difficult to determine which residues were hydrogen bonded to each other and which cross peaks arose from spin diffusion. In contrast to the study of regular, globular proteins by NOE methods, shortening the mixing time proved not to be an effective method for reducing spin diffusion; such shortening simply results in an almost homogeneous attenuation of all cross peaks due to the smaller fraction of peptides forming oligomeric species, whereas the large heterogeneity in oligomer sizes persists.

By examining cross peak intensities, we have identified three hydrogen bonds: V18-M35, F20-G33, and E22-I31. These are consistent with an antiparallel β-sheet (Fig. 12B). Although it remained unclear from this data alone whether these hydrogen bonds were intra- or intermolecular, mixed labeling identified them to be intramolecular (data not shown). Interestingly, this hydrogen-bonding pattern is identical to that reported for a monomeric structure of $A\beta_{40}$ bound to an affibody (Hoyer et al., 2008), suggesting that the affibody-bound structure indeed represents the monomeric structure of $A\beta_{40}$ within oligomers. This intramolecular, antiparallel hydrogen bonding motif for the oligomer is in stark contrast to the cross-β parallel, in-register structures reported for $A\beta_{40}$ fibrils (Paravastu et al., 2008). The hydrogen bonding axis is rotated by 90°, meaning that to go from the oligomeric state to the fibrillar state, all backbone hydrogen bonds must be broken and reformed, which represents a significant energetic barrier between these two states.

7.3 Measurement of intermolecular sidechain methyl to backbone amide NOEs on oligomeric $A\beta_{40}$

Although the amide-amide NOESY spectra yielded valuable information on the hydrogen bonding pattern within $A\beta_{40}$ oligomers, they did not provide information on contacts between planes perpendicular to the hydrogen bonds and thus provided insufficient structural restraints to determine the quaternary structure of the oligomeric species. To obtain such intermolecular NOEs we recorded a pressure-jump 3D ^{13}C-^{15}N-^{1}H

HMQC-NOESY-HSQC spectrum (Ciudad et al., 2020) on a mixed-labeled sample in which two thirds of the peptide had protonated and ^{13}C-labeled methyl groups for isoleucine, leucine, and valine (ILV) in an otherwise deuterated background and natural abundance nitrogen while one third of the peptide was ^{2}H,^{15}N-labeled. With this mixed isotopic labeling scheme all cross peaks that show up in the NOESY spectrum inherently represent intermolecular contacts between methyl sidechain protons and backbone amide protons, potentially providing contacts between different β-sheets.

Under static high-pressure conditions (2.4 kbar), the ILV methyl groups of $A\beta_{40}$ yield a ^{1}H-^{13}C HMQC spectrum with characteristic random coil chemical shifts (Fig. 13A). Despite the limited chemical shift dispersion, particularly in the proton dimension, most of the resonances were well-resolved and can be assigned based on previously published reports (Hou et al., 2004; Yan et al., 2007); only the I31 and I32 C^{δ} methyl groups were completely overlapped. To decrease the size of the ^{13}C spectral window and make it possible to acquire very high-resolution spectra with fewer points in the ^{13}C dimension, the indirect dimension of the HMQC spectrum was folded twice (Fig. 13A, Right). While folding the spectrum greatly decreased the spectral width needed to acquire the HMQC, most peaks remain well-resolved in the ^{13}C dimension.

The pressure jump 3D ^{13}C-^{15}N-^{1}H HMQC-NOESY-HSQC pulse sequence is similar to the ^{15}N-^{15}N-^{1}H HMQC-NOESY-HMQC pulse sequence (Fig. 11A) except that the initial ^{1}H-^{15}N HMQC is replaced with a ^{1}H-^{13}C HMQC element. Magnetization is subsequently transferred from methyl side-chain protons to backbone amides during a NOE mixing period before a high-sensitivity ^{1}H-^{15}N HSQC read-out. A 60-ms low-pressure period was included during the 140-ms NOE mixing period to allow the $A\beta_{40}$ to oligomerize and to generate NOEs in the oligomeric state. To obtain the highest possible spectral resolution, this experiment was carried out at 900-MHz, using rather long ^{15}N and ^{13}C evolution times of 49.8 ms and 51.7 ms, respectively. With 4.2 % time-ordered NUS sampling and a four-step phase cycle, 400 FIDs were collected, corresponding to 1600 pressure cycles and a total experimental time of ~4 h.

Numerous NOE cross peaks were observed for residues that are within the rigid core of the $A\beta_{40}$ oligomer (L17-V40) (Fig. 13B). Because the sample had a mixed isotopic labeling scheme, with either the methyls being protonated and ^{13}C-labeled or the backbone ^{15}N being labeled, all cross peaks that show up in this spectrum must be intermolecular in nature. These

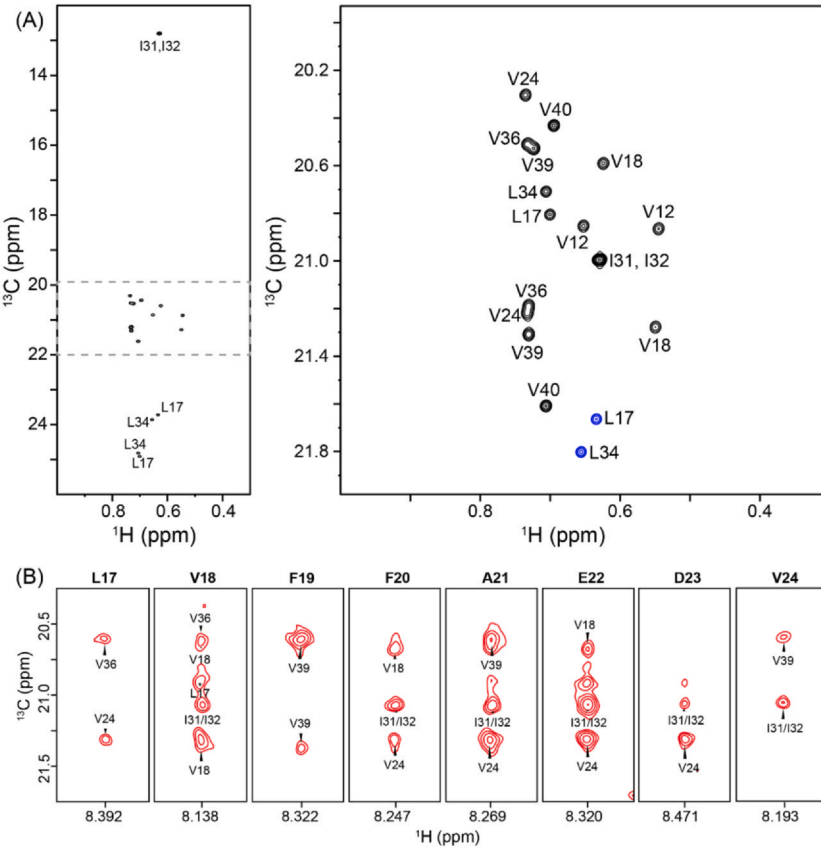

Fig. 13 Sidechain methyl to backbone NOEs for oligomeric $A\beta_{40}$. (A) (Left) Full ^{1}H-^{13}C HMQC spectrum for ILV-labeled $A\beta_{40}$ at 2.4 kbar. (Right) Folded HMQC spectrum where the indirect dimension is folded twice to greatly enhance ^{13}C spectral resolution for the same number of sampled data points. Black contours represent positive signal while blue contours represent negative signal due to being folded an odd number of times into the spectrum. (B) Strip plots from the pressure-jump 3D ^{13}C-^{15}N-^{1}H HMQC-NOESY-HSQC spectrum on 2:1 ^{2}H,ILV:^{2}H,^{15}N labeled $A\beta_{40}$ in 50 mM sodium acetate buffer, pH 4.5, with 5 mM NaCl, 1 mM EDTA, and 3 % D_2O.

intermolecular cross peaks therefore contain a wealth of information on the quaternary packing of monomers within the $A\beta_{40}$ oligomers. However, just as there was extensive spin diffusion in the backbone-to-backbone amide ^{15}N-^{15}N-^{1}H HMQC-NOESY-HMQC spectrum, this methyl sidechain to backbone amide ^{13}C-^{15}N-^{1}H HMQC-NOESY-HSQC spectrum also displays significant spin diffusion. For example, there is a stretch where NOEs are observed from V24's methyl to the backbone amides of F20, A21, E22,

and D23. Additionally, there is an NOE from V24 to L17 which may be a separate contact but could also be part of this extensive spin diffusion network. Spin diffusion makes it intractable to directly assign any of the intermolecular cross peaks to direct contacts; observed cross peaks may be due to a direct contact but also may be due to spin diffusion from neighboring residues. In contrast to NOE studies of regular folded proteins, shortening the NOE mixing period (or the low-pressure duration) does not significantly reduce the effect of spin diffusion but primarily lowers all NOE intensities. The reason for this counter-intuitive behavior is rooted in the very heterogenous distribution of oligomer sizes, where only the largest ones exhibit rapid NOE transfer but also spin diffusion, thus compromising the structural interpretation of NOEs.

8. Conclusions

There is growing evidence that Aβ oligomers are one of the primary toxic species responsible for the debilitating symptoms of Alzheimer's disease. $A\beta_{40}$ oligomers are inherently difficult to study on a residue-specific level due to their transient nature and intermediate, heterogeneous size. Pressure-jump NMR spectroscopy is uniquely well-suited for the study of these otherwise NMR-invisible oligomers and provides a wealth of information on their structure and kinetics. ^{15}N T_1 relaxation times report on which residues are highly ordered and suggest that residues V18-A21 and I31-L34 of $A\beta_{40}$ make up β-sheets, while the N-terminal 10 residues remain dynamically disordered in the oligomeric state. However, the presence of Zn^{2+} during oligomerization causes substantial rigidification of these N-terminal residues and further reduces the internal dynamics of the β-sheet region. ^{15}N transverse relaxation times report on the size of the oligomers produced. Under the conditions used for these experiments, the $A\beta_{40}$ oligomers grow to the size of an ~80-mer within 1.25 s and continue to grow to an average size of a ~300-mer 3.75 s after a drop to atmospheric pressure. After a certain number of pressure cycles, monomeric $A\beta_{40}$ is converted into pressure-resistant fibrils, thus limiting the number of pressure cycles that can be used for any individual pressure-jump NMR experiment. Amelotin, on the other hand, only formed pressure-resistant aggregates after a few hundred thousand pressure cycles, yet still forms pressure-sensitive oligomers whose structure can be probed by pressure-jump NMR. Techniques developed on amelotin to measure secondary shifts and NOEs in the oligomeric state are readily

applicable to $A\beta_{40}$ and other oligomeric systems. Backbone-to-backbone amide ^{1}H-^{1}H NOEs of oligomeric $A\beta_{40}$ revealed hydrogen bonds between V18 and M35, F20 and G33, and E22 and I31. This hydrogen bonding motif is the same as was previously observed for affibody-bound monomeric $A\beta_{40}$, suggesting that monomers within the oligomeric state have the same structure as the affibody-bound $A\beta_{40}$. In contrast to the study of regular, well-defined monomeric or oligomeric proteins by solution state NMR, NOE contacts for $A\beta_{40}$ contain extensive spin diffusion contributions that result from the highly heterogeneous size of the oligomers and cannot be effectively mitigated by shortening NOE mixing times. Consequently, distance restraints derived from NOE data must be treated with caution. Although numerous methyl to amide intermolecular NOEs were also observed, the conformational space for packing folded monomers into an oligomeric quaternary arrangement is enormous. Solving the atomic resolution structure of $A\beta_{40}$ therefore will require further methodological development, both in terms of computation and for reducing the effects of spin diffusion, possibly by more selective isotope labeling protocols.

Acknowledgments

We thank James L. Baber, Jinfa Ying, John Louis, and Sean Fitch for experimental assistance, and Angus Robertson and Ashley Barnes for helpful discussions. This research was supported by the Intramural Research Program of the National Institute of Diabetes and Digestive and Kidney Diseases (NIDDK) within the National Institutes of Health (NIH). The contributions of the NIH authors are considered Works of the United States Government. The findings and conclusions presented in this paper are those of the authors and do not necessarily reflect the views of the NIH or the U.S. Department of Health and Human Services.

References

Abbarin, N., San Miguel, S., Holcroft, J., Iwasaki, K., & Ganss, B. (2015). The enamel protein amelotin is a promoter of hydroxyapatite mineralization. *Journal of Bone and Mineral Research, 30*(5), 775–785. https://doi.org/10.1002/jbmr.2411.

Abelein, A., Gräslund, A., & Danielsson, J. (2015). Zinc as chaperone-mimicking agent for retardation of amyloid β peptide fibril formation. *Proceedings of the National Academy of Sciences of the United States of America, 112*(17), 5407–5412. https://doi.org/10.1073/pnas.1421961112.

Abyzov, A., Salvi, N., Schneider, R., Maurin, D., Ruigrok, R. W. H., Jensen, M. R., & Blackledge, M. (2016). Identification of dynamic modes in an intrinsically disordered protein using temperature-dependent NMR relaxation. *Journal of the American Chemical Society, 138*(19), 6240–6251. https://doi.org/10.1021/jacs.6b02424.

Alderson, T. R., Charlier, C., Torchia, D. A., Anfinrud, P., & Bax, A. (2017). Monitoring hydrogen exchange during protein folding by fast pressure jump NMR spectroscopy. *Journal of the American Chemical Society, 139*(32), 11036–11039. https://doi.org/10.1021/jacs.7b06676.

Amin, L., & Harris, D. A. (2021). Aβ receptors specifically recognize molecular features displayed by fibril ends and neurotoxic oligomers. *Nature Communications, 12*(1), 3451. https://doi.org/10.1038/s41467-021-23507-z.

Arispe, N., Rojas, E., & Pollard, H. B. (1993). Alzheimer disease amyloid beta protein forms calcium channels in bilayer membranes: Blockade by tromethamine and aluminum. *Proceedings of the National Academy of Sciences, 90*(2), 567–571. https://doi.org/10.1073/pnas.90.2.567.

Barna, J. C. J., Laue, E. D., Mayger, M. R., Skilling, J., & Worrall, S. J. P. (1987). Exponential sampling, an alternative method for sampling in two-dimensional NMR experiments. *Journal of Magnetic Resonance (1969), 73*(1), 69–77. https://doi.org/10.1016/0022-2364(87)90225-3.

Barnes, C. A., Robertson, A. J., Louis, J. M., Anfinrud, P., & Bax, A. (2019). Observation of β-Amyloid peptide oligomerization by pressure-jump NMR spectroscopy. *Journal of the American Chemical Society, 141*(35), 13762–13766. https://doi.org/10.1021/jacs.9b06970.

Berjanskii, M. V., & Wishart, D. S. (2005). A simple method to predict protein flexibility using secondary chemical shifts. *Journal of the American Chemical Society, 127*(43), 14970–14971. https://doi.org/10.1021/ja054842f.

Bertini, I., Gonnelli, L., Luchinat, C., Mao, J., & Nesi, A. (2011). A new structural model of Aβ40 fibrils. *Journal of the American Chemical Society, 133*(40), 16013–16022. https://doi.org/10.1021/ja2035859.

Blömeke, L., Rehn, F., Kraemer-Schulien, V., Kutzsche, J., Pils, M., Bujnicki, T., ... Hansen, N., ... Peters, O. (2024). Aβ oligomers peak in early stages of Alzheimer's disease preceding tau pathology. *Alzheimer's & Dementia: Diagnosis, Assessment & Disease Monitoring, 16*(2), e12589. https://doi.org/10.1002/dad2.12589.

Campioni, S., Mannini, B., Zampagni, M., Pensalfini, A., Parrini, C., Evangelisti, E., ... Chiti, F. (2010). A causative link between the structure of aberrant protein oligomers and their toxicity. *Nature Chemical Biology, 6*(2), 140–147. https://doi.org/10.1038/nchembio.283.

Caro, J. A., & Wand, A. J. (2018). Practical aspects of high-pressure NMR spectroscopy and its applications in protein biophysics and structural biology. *Methods (San Diego, Calif.), 148*, 67–80. https://doi.org/10.1016/j.ymeth.2018.06.012.

Cawood, E. E., Karamanos, T. K., Wilson, A. J., & Radford, S. E. (2021). Visualizing and trapping transient oligomers in amyloid assembly pathways. *Biophysical Chemistry, 268*, 106505. https://doi.org/10.1016/j.bpc.2020.106505.

Charlier, C., Alderson, T. R., Courtney, J. M., Ying, J., Anfinrud, P., & Bax, A. (2018a). Study of protein folding under native conditions by rapidly switching the hydrostatic pressure inside an NMR sample cell. *Proceedings of the National Academy of Sciences, 115*(18), E4169–E4178. https://doi.org/10.1073/pnas.1803642115.

Charlier, C., Courtney, J. M., Alderson, T. R., Anfinrud, P., & Bax, A. (2018b). Monitoring 15N chemical shifts during protein folding by pressure-jump NMR. *Journal of the American Chemical Society, 140*(26), 8096–8099. https://doi.org/10.1021/jacs.8b04833.

Charlier, C., Courtney, J. M., Anfinrud, P., & Bax, A. (2018c). Interrupted pressure-jump NMR experiments reveal resonances of on-pathway protein folding intermediate. *The Journal of Physical Chemistry. B, 122*(49), 11792–11799. https://doi.org/10.1021/acs.jpcb.8b08456.

Chiliveri, S. C., Robertson, A. J., Shen, Y., Torchia, D. A., & Bax, A. (2022). Advances in NMR spectroscopy of weakly aligned biomolecular systems. *Chemical Reviews, 122*(10), 9307–9330. https://doi.org/10.1021/acs.chemrev.1c00730.

Chiliveri, S. C., Shen, Y., Baber, J. L., Ying, J., Sagar, V., Wistow, G., ... Bax, A. (2023). Experimental NOE, chemical shift, and proline isomerization data provide detailed insights into amelotin oligomerization. *Journal of the American Chemical Society, 145*(32), 18063–18074. https://doi.org/10.1021/jacs.3c05710.

Chung, H. S. (2024). Characterizing heterogeneity in amyloid formation processes. *Current Opinion in Structural Biology, 89*, 102951. https://doi.org/10.1016/j.sbi.2024.102951.

Ciudad, S., Puig, E., Botzanowski, T., Meigooni, M., Arango, A. S., Do, J., ... Carulla, N. (2020). Aβ(1-42) tetramer and octamer structures reveal edge conductivity pores as a mechanism for membrane damage. *Nature Communications, 11*(1), 3014. https://doi.org/10.1038/s41467-020-16566-1.

Cohen, S. I. A., Cukalevski, R., Michaels, T. C. T., Šarić, A., Törnquist, M., Vendruscolo, M., ... Linse, S. (2018). Distinct thermodynamic signatures of oligomer generation in the aggregation of the amyloid-β peptide. *Nature Chemistry, 10*(5), 523–531. https://doi.org/10.1038/s41557-018-0023-x.

Cole, H. B. R., & Torchia, D. A. (1991). An NMR study of the backbone dynamics of staphylococcal nuclease in the crystalline state. *Chemical Physics, 158*(2), 271–281. https://doi.org/10.1016/0301-0104(91)87071-3.

Culik, R. M., Sekhar, A., Nagesh, J., Deol, H., Rumfeldt, J. A. O., Meiering, E. M., & Kay, L. E. (2018). Effects of maturation on the conformational free-energy landscape of SOD1. *Proceedings of the National Academy of Sciences, 115*(11), E2546–E2555. https://doi.org/10.1073/pnas.1721022115.

Danielsson, J., Pierattelli, R., Banci, L., & Gräslund, A. (2007). High-resolution NMR studies of the zinc-binding site of the Alzheimer's amyloid β-peptide. *The FEBS Journal, 274*(1), 46–59. https://doi.org/10.1111/j.1742-4658.2006.05563.x.

de Dios, A. C., Pearson, J. G., & Oldfield, E. (1993). Secondary and tertiary structural effects on protein NMR chemical shifts: An ab initio approach. *Science (New York, N. Y.), 260*(5113), 1491–1496. https://doi.org/10.1126/science.8502992.

Dear, A. J., Michaels, T. C. T., Meisl, G., Klenerman, D., Wu, S., Perrett, S., ... Knowles, T. P. J. (2020). Kinetic diversity of amyloid oligomers. *Proceedings of the National Academy of Sciences, 117*(22), 12087–12094. https://doi.org/10.1073/pnas.1922267117.

Demuro, A., Smith, M., & Parker, I. (2011). Single-channel Ca2+ imaging implicates Aβ1–42 amyloid pores in Alzheimer's disease pathology. *Journal of Cell Biology, 195*(3), 515–524. https://doi.org/10.1083/jcb.201104133.

Dill, K. A., & Chan, H. S. (1997). From Levinthal to pathways to funnels. *Nature Structural Biology, 4*(1), 10–19. https://doi.org/10.1038/nsb0197-10.

Dyson, H. J., & Wright, P. E. (2017). How does your protein fold? elucidating the apomyoglobin folding pathway. *Accounts of Chemical Research, 50*(1), 105–111. https://doi.org/10.1021/acs.accounts.6b00511.

Evans, R., O'Neill, M., Pritzel, A., Antropova, N., Senior, A., Green, T., & Hassabis, D. (2022). *Protein complex prediction with AlphaFold-Multimer* (p. 2021.10.04.463034). bioRxiv. https://doi.org/10.1101/2021.10.04.463034.

Eykyn, T. R., & Kuchel, P. W. (2003). Scalar couplings as pH probes in compartmentalized biological systems: ^{31}P NMR of phosphite. *Magnetic Resonance in Medicine, 50*(4), 693–696. https://doi.org/10.1002/mrm.10580.

Fani, G., Mannini, B., Vecchi, G., Cascella, R., Cecchi, C., Dobson, C. M., ... Chiti, F. (2021). Aβ oligomers dysregulate calcium homeostasis by mechanosensitive activation of AMPA and NMDA receptors. *ACS Chemical Neuroscience, 12*(4), 766–781. https://doi.org/10.1021/acschemneuro.0c00811.

Fawzi, N. L., Ying, J., Ghirlando, R., Torchia, D. A., & Clore, G. M. (2011). Atomic-resolution dynamics on the surface of amyloid-β protofibrils probed by solution NMR. *Nature, 480*(7376), 268–272. https://doi.org/10.1038/nature10577.

Fawzi, N. L., Ying, J., Torchia, D. A., & Clore, G. M. (2012). Probing exchange kinetics and atomic resolution dynamics in high-molecular-weight complexes using dark-state exchange saturation transfer NMR spectroscopy. *Nature Protocols, 7*(8), 1523–1533. https://doi.org/10.1038/nprot.2012.077.

Fitch, S. (2025). *SeanIFitch/icarus_v2* [Python]. https://github.com/SeanIFitch/icarus_v2 (Original work published 2024).

Foguel, D., Suarez, M. C., Ferrão-Gonzales, A. D., Porto, T. C. R., Palmieri, L., Einsiedler, C. M., ... Silva, J. L. (2003). Dissociation of amyloid fibrils of α-synuclein and transthyretin by pressure reveals their reversible nature and the formation of water-excluded cavities. *Proceedings of the National Academy of Sciences, 100*(17), 9831–9836. https://doi.org/10.1073/pnas.1734009100.

Folmer, R. H. A., Hilbers, C. W., Konings, R. N. H., & Hallenga, K. (1995). A 13C double-filtered NOESY with strongly reduced artefacts and improved sensitivity. *Journal of Biomolecular NMR, 5*(4), 427–432. https://doi.org/10.1007/BF00182287.

Fouillen, A., Dos Santos Neves, J., Mary, C., Castonguay, J.-D., Moffatt, P., Baron, C., & Nanci, A. (2017). Interactions of AMTN, ODAM and SCPPPQ1 proteins of a specialized basal lamina that attaches epithelial cells to tooth mineral. *Scientific Reports, 7*(1), 46683. https://doi.org/10.1038/srep46683.

Frenkiel, T., Bauer, C., Carr, M. D., Birdsall, B., & Feeney, J. (1990). HMQC-NOESY-HMQC, a three-dimensional NMR experiment which allows detection of nuclear overhauser effects between protons with overlapping signals. *Journal of Magnetic Resonance (1969), 90*(2), 420–425. https://doi.org/10.1016/0022-2364(90)90152-Y.

Friedrich, D., Perodeau, J., Nieuwkoop, A. J., & Oschkinat, H. (2020). MAS NMR detection of hydrogen bonds for protein secondary structure characterization. *Journal of Biomolecular NMR, 74*(4), 247–256. https://doi.org/10.1007/s10858-020-00307-z.

Frieg, B., Han, M., Giller, K., Dienemann, C., Riedel, D., Becker, S., ... Schröder, G. F. (2024). Cryo-EM structures of lipidic fibrils of amyloid-β (1-40). *Nature Communications, 15*(1), 1297. https://doi.org/10.1038/s41467-023-43822-x.

Geierstanger, B., Jamin, M., Volkman, B. F., & Baldwin, R. L. (1998). Protonation behavior of histidine 24 and histidine 119 in forming the pH 4 folding intermediate of apomyoglobin. *Biochemistry, 37*(12), 4254–4265. https://doi.org/10.1021/bi972516+.

Gelenter, M. D., & Bax, A. (2023). Recombinant expression and chemical amidation of isotopically labeled native melittin. *Journal of the American Chemical Society, 145*(7), 3850–3854. https://doi.org/10.1021/jacs.2c12631.

Gelenter, M. D., Yau, W.-M., Anfinrud, P. A., & Bax, A. (2024). From milliseconds to minutes: Melittin self-assembly from concerted non-equilibrium pressure-jump and equilibrium relaxation nuclear magnetic resonance. *The Journal of Physical Chemistry Letters, 15*(7), 1930–1935. https://doi.org/10.1021/acs.jpclett.3c03563.

Hahn, E. L. (1950). Spin Echoes. *Physical Review, 80*(4), 580–594. https://doi.org/10.1103/PhysRev.80.580.

Hansen, A. L., & Brüschweiler, R. (2016). Absolute minimal sampling in high-dimensional NMR spectroscopy. *Angewandte Chemie International Edition, 55*(45), 14169–14172. https://doi.org/10.1002/anie.201608048.

Herrmann, T., Güntert, P., & Wüthrich, K. (2002). Protein NMR structure determination with automated NOE-identification in the NOESY spectra using the new software ATNOS. *Journal of Biomolecular NMR, 24*(3), 171–189. https://doi.org/10.1023/a:1021614115432.

Horst, R., Wider, G., Fiaux, J., Bertelsen, E. B., Horwich, A. L., & Wüthrich, K. (2006). Proton–proton overhauser NMR spectroscopy with polypeptide chains in large structures. *Proceedings of the National Academy of Sciences, 103*(42), 15445–15450. https://doi.org/10.1073/pnas.0607141103.

Hou, L., Shao, H., Zhang, Y., Li, H., Menon, N. K., Neuhaus, E. B., ... Zagorski, M. G. (2004). Solution NMR studies of the Aβ(1−40) and Aβ(1−42) peptides establish that the Met35 oxidation state affects the mechanism of amyloid formation. *Journal of the American Chemical Society, 126*(7), 1992–2005. https://doi.org/10.1021/ja036813f.

Hoyer, W., Grönwall, C., Jonsson, A., Ståhl, S., & Härd, T. (2008). Stabilization of a β-hairpin in monomeric Alzheimer's amyloid-β peptide inhibits amyloid formation. *Proceedings of the National Academy of Sciences, 105*(13), 5099–5104. https://doi.org/10.1073/pnas.0711731105.

Hwang, P. M., Choy, W.-Y., Lo, E. I., Chen, L., Forman-Kay, J. D., Raetz, C. R. H., ... Kay, L. E. (2002). Solution structure and dynamics of the outer membrane enzyme PagP by NMR. *Proceedings of the National Academy of Sciences, 99*(21), 13560–13565. https://doi.org/10.1073/pnas.212344499.

Ikura, M., Bax, A., Clore, G. M., & Gronenborn, A. M. (1990). Detection of nuclear Overhauser effects between degenerate amide proton resonances by heteronuclear three-dimensional NMR spectroscopy. *Journal of the American Chemical Society, 112*(24), 9020–9022. https://doi.org/10.1021/ja00180a080.

Jumper, J., Evans, R., Pritzel, A., Green, T., Figurnov, M., Ronneberger, O., ... Adler, J., ... Hassabis, D. (2021). Highly accurate protein structure prediction with AlphaFold. Article 7873 *Nature, 596*(7873), https://doi.org/10.1038/s41586-021-03819-2.

Kamatari, Y. O., Kitahara, R., Yamada, H., Yokoyama, S., & Akasaka, K. (2004). High-pressure NMR spectroscopy for characterizing folding intermediates and denatured states of proteins. *Methods (San Diego, Calif.), 34*(1), 133–143. https://doi.org/10.1016/j.ymeth.2004.03.010.

Karamanos, T. K., Kalverda, A. P., Thompson, G. S., & Radford, S. E. (2015). Mechanisms of amyloid formation revealed by solution NMR. *Progress in Nuclear Magnetic Resonance Spectroscopy, 0*, 86–104. https://doi.org/10.1016/j.pnmrs.2015.05.002.

Kay, L. E., Keifer, P., & Saarinen, T. (1992). Pure absorption gradient enhanced heteronuclear single quantum correlation spectroscopy with improved sensitivity. *Journal of the American Chemical Society, 114*(26), 10663–10665. https://doi.org/10.1021/ja00052a088.

Kotler, S. A., Tugarinov, V., Schmidt, T., Ceccon, A., Libich, D. S., Ghirlando, R., ... Clore, G. M. (2019). Probing initial transient oligomerization events facilitating Huntingtin fibril nucleation at atomic resolution by relaxation-based NMR. *Proceedings of the National Academy of Sciences, 116*(9), 3562–3571. https://doi.org/10.1073/pnas.1821216116.

Kremer, W., Arnold, M., Munte, C. E., Hartl, R., Erlach, M. B., Koehler, J., ... Kalbitzer, H. R. (2011). Pulsed pressure perturbations, an extra dimension in NMR spectroscopy of proteins. *Journal of the American Chemical Society, 133*(34), 13646–13651. https://doi.org/10.1021/ja2050698.

Kupče, E., & Freeman, R. (2007). SPEED: Single-point evaluation of the evolution dimension. *Magnetic Resonance in Chemistry, 45*(9), 711–713. https://doi.org/10.1002/mrc.2052.

Lee, W., Revington, M. J., Arrowsmith, C., & Kay, L. E. (1994). A pulsed field gradient isotope-filtered 3D 13C HMQC-NOESY experiment for extracting intermolecular NOE contacts in molecular complexes. *FEBS Letters, 350*(1), 87–90. https://doi.org/10.1016/0014-5793(94)00740-3.

LeMaster, D. M. (1989). [2] Deuteration in protein proton magnetic resonance (Academic Press) *In Methods in Enzymology, 177*, 23–43. https://doi.org/10.1016/0076-6879(89)77004-X.

Lipari, G., & Szabo, A. (1982). Model-free approach to the interpretation of nuclear magnetic resonance relaxation in macromolecules. 1. Theory and range of validity. *Journal of the American Chemical Society, 104*(17), 4546–4559. https://doi.org/10.1021/ja00381a009.

Masoumzadeh, E., Ying, J., Baber, J. L., Anfinrud, P., & Bax, A. (2024). Proline peptide bond isomerization in ubiquitin under folding and denaturing conditions by pressure-jump NMR. *Journal of Molecular Biology, 436*(11), 168587. https://doi.org/10.1016/j.jmb.2024.168587.

Meng, F., Bellaiche, M. M. J., Kim, J.-Y., Zerze, G. H., Best, R. B., & Chung, H. S. (2018). Highly disordered Amyloid-β monomer probed by single-molecule FRET and MD simulation. *Biophysical Journal, 114*(4), 870–884. https://doi.org/10.1016/j.bpj.2017.12.025.

Miller, L. M., Wang, Q., Telivala, T. P., Smith, R. J., Lanzirotti, A., & Miklossy, J. (2006). Synchrotron-based infrared and X-ray imaging shows focalized accumulation of Cu and Zn co-localized with β-amyloid deposits in Alzheimer's disease. *Journal of Structural Biology, 155*(1), 30–37. https://doi.org/10.1016/j.jsb.2005.09.004.

Minicozzi, V., Stellato, F., Comai, M., Dalla Serra, M., Potrich, C., Meyer-Klaucke, W., & Morante, S. (2008). Identifying the minimal copper- and zinc-binding site sequence in amyloid-beta peptides. *The Journal of Biological Chemistry, 283*(16), 10784–10792. https://doi.org/10.1074/jbc.M707109200.

Orekhov, V., Yu, & Jaravine, V. A. (2011). Analysis of non-uniformly sampled spectra with multi-dimensional decomposition. *Progress in Nuclear Magnetic Resonance Spectroscopy, 59*(3), 271–292. https://doi.org/10.1016/j.pnmrs.2011.02.002.

Paladini, A. A., Jr., & Weber, G. (1981). Pressure-induced reversible dissociation of enolase. *Biochemistry, 20*(9), 2587–2593. https://doi.org/10.1021/bi00512a034.

Paravastu, A. K., Leapman, R. D., Yau, W.-M., & Tycko, R. (2008). Molecular structural basis for polymorphism in Alzheimer's β-amyloid fibrils. *Proceedings of the National Academy of Sciences, 105*(47), 18349–18354. https://doi.org/10.1073/pnas.0806270105.

Peterson, R. W., & Wand, A. J. (2005). Self-contained high-pressure cell, apparatus, and procedure for the preparation of encapsulated proteins dissolved in low viscosity fluids for nuclear magnetic resonance spectroscopy. *Review of Scientific Instruments, 76*(9), 094101. https://doi.org/10.1063/1.2038087.

Petkova, A. T., Ishii, Y., Balbach, J. J., Antzutkin, O. N., Leapman, R. D., Delaglio, F., & Tycko, R. (2002). A structural model for Alzheimer's β-amyloid fibrils based on experimental constraints from solid state NMR. *Proceedings of the National Academy of Sciences, 99*(26), 16742–16747. https://doi.org/10.1073/pnas.262663499.

Phillips, J. C. (2019). Why Aβ42 Is much more toxic than Aβ40. *ACS Chemical Neuroscience, 10*(6), 2843–2847. https://doi.org/10.1021/acschemneuro.9b00068.

Piotto, M., Saudek, V., & Sklenář, V. (1992). Gradient-tailored excitation for single-quantum NMR spectroscopy of aqueous solutions. *Journal of Biomolecular NMR, 2*(6), 661–665. https://doi.org/10.1007/BF02192855.

Rachline, J., Perin-Dureau, F., Goff, A. L., Neyton, J., & Paoletti, P. (2005). The micromolar zinc-binding domain on the NMDA receptor subunit NR2B. *Journal of Neuroscience, 25*(2), 308–317. https://doi.org/10.1523/JNEUROSCI.3967-04.2005.

Ren, X., Zhou, M., Mu, Y., & Tian, K. (2021). Amelotin-mediated crystals assembly in liquid-phase and on tooth surface. *Journal of Materials Science and Chemical Engineering, 9*(7), https://doi.org/10.4236/msce.2021.97004.

Roche, J., Royer, C. A., & Roumestand, C. (2017). Monitoring protein folding through high pressure NMR spectroscopy. *Progress in Nuclear Magnetic Resonance Spectroscopy, 102–103*, 15–31. https://doi.org/10.1016/j.pnmrs.2017.05.003.

Rohl, C. A., & Baker, D. (2002). De Novo determination of protein backbone structure from residual dipolar couplings using rosetta. *Journal of the American Chemical Society, 124*(11), 2723–2729. https://doi.org/10.1021/ja016880e.

Rovnyak, D., Frueh, D. P., Sastry, M., Sun, Z.-Y. J., Stern, A. S., Hoch, J. C., & Wagner, G. (2004). Accelerated acquisition of high resolution triple-resonance spectra using non-uniform sampling and maximum entropy reconstruction. *Journal of Magnetic Resonance, 170*(1), 15–21. https://doi.org/10.1016/j.jmr.2004.05.016.

Sachse, C., Fändrich, M., & Grigorieff, N. (2008). Paired β-sheet structure of an Aβ(1-40) amyloid fibril revealed by electron microscopy. *Proceedings of the National Academy of Sciences, 105*(21), 7462–7466. https://doi.org/10.1073/pnas.0712290105.

Sanz-Blasco, S., Valero, R. A., Rodríguez-Crespo, I., Villalobos, C., & Núñez, L. (2008). Mitochondrial Ca2+ overload underlies Aβ oligomers neurotoxicity providing an unexpected mechanism of neuroprotection by NSAIDs. *PLoS One, 3*(7), e2718. https://doi.org/10.1371/journal.pone.0002718.

Schanda, P., Meier, B. H., & Ernst, M. (2010). Quantitative analysis of protein backbone dynamics in microcrystalline ubiquitin by solid-state NMR spectroscopy. *Journal of the American Chemical Society, 132*(45), 15957–15967. https://doi.org/10.1021/ja100726a.

Schützmann, M. P., Hasecke, F., Bachmann, S., Zielinski, M., Hänsch, S., Schröder, G. F., ... Hoyer, W. (2021). Endo-lysosomal Aβ concentration and pH trigger formation of Aβ oligomers that potently induce Tau missorting. *Nature Communications, 12*(1), 4634. https://doi.org/10.1038/s41467-021-24900-4.

Shaka, A. J., Barker, P. B., & Freeman, R. (1985). Computer-optimized decoupling scheme for wideband applications and low-level operation. *Journal of Magnetic Resonance (1969), 64*(3), 547–552. https://doi.org/10.1016/0022-2364(85)90122-2.

Shen, F., Regmi, D., Islam, M., Raja Somu, D., Merk, V., & Du, D. (2022). Effects of zinc and carnosine on aggregation kinetics of Amyloid-β40 peptide. *Biochemistry and Biophysics Reports, 32*, 101333. https://doi.org/10.1016/j.bbrep.2022.101333.

Shen, Y., & Bax, A. (2015). Protein structural information derived from NMR chemical shift with the neural network program TALOS-N. In H. Cartwright (Ed.). *Artificial Neural Networks* (pp. 17–32) Springer. https://doi.org/10.1007/978-1-4939-2239-0_2.

Solomonov, I., Korkotian, E., Born, B., Feldman, Y., Bitler, A., Rahimi, F., ... Sagi, I. (2012). Zn2+-Aβ40 complexes form metastable quasi-spherical oligomers that are cytotoxic to cultured hippocampal neurons. *Journal of Biological Chemistry, 287*(24), 20555–20564. https://doi.org/10.1074/jbc.M112.344036.

Tang, H., Andrikopoulos, N., Li, Y., Ke, S., Sun, Y., Ding, F., & Ke, P. C. (2025). Emerging biophysical origins and pathogenic implications of amyloid oligomers. *Nature Communications, 16*(1), 2937. https://doi.org/10.1038/s41467-025-58335-y.

Thinakaran, G., & Koo, E. H. (2008). Amyloid precursor protein trafficking, processing, and function. *Journal of Biological Chemistry, 283*(44), 29615–29619. https://doi.org/10.1074/jbc.R800019200.

Torchia, D. A., Sparks, S. W., & Bax, A. (1988). Delineation of.alpha.-helical domains in deuteriated Staphylococcal nuclease by 2D NOE NMR spectroscopy. *Journal of the American Chemical Society, 110*(7), 2320–2321. https://doi.org/10.1021/ja00215a063.

Tosatto, L., Horrocks, M. H., Dear, A. J., Knowles, T. P. J., Dalla Serra, M., Cremades, N., ... Klenerman, D. (2015). Single-molecule FRET studies on alpha-synuclein oligomerization of Parkinson's disease genetically related mutants. *Scientific Reports, 5*(1), 16696. https://doi.org/10.1038/srep16696.

Tugarinov, V., Kanelis, V., & Kay, L. E. (2006). Isotope labeling strategies for the study of high-molecular-weight proteins by solution NMR spectroscopy. *Nature Protocols, 1*(2), 749–754. https://doi.org/10.1038/nprot.2006.101.

Wishart, D. S., & Sykes, B. D. (1994). The 13C chemical-shift index: A simple method for the identification of protein secondary structure using 13C chemical-shift data. *Journal of Biomolecular NMR, 4*(2), 171–180. https://doi.org/10.1007/BF00175245.

Yan, Y., Liu, J., McCallum, S. A., Yang, D., & Wang, C. (2007). Methyl dynamics of the amyloid-β peptides Aβ40 and Aβ42. *Biochemical and Biophysical Research Communications, 362*(2), 410–414. https://doi.org/10.1016/j.bbrc.2007.07.198.

Yang, Y., Murzin, A. G., Peak-Chew, S., Franco, C., Garringer, H. J., Newell, K. L., ... Scheres, S. H. W. (2023). Cryo-EM structures of Aβ40 filaments from the leptomeninges of individuals with Alzheimer's disease and cerebral amyloid angiopathy. *Acta Neuropathologica Communications, 11*(1), 191. https://doi.org/10.1186/s40478-023-01694-8.

Ying, J., Barnes, C. A., Louis, J. M., & Bax, A. (2019). Importance of time-ordered non-uniform sampling of multi-dimensional NMR spectra of Aβ1–42 peptide under aggregating conditions. *Journal of Biomolecular NMR, 73*(8–9), 429–441. https://doi.org/10.1007/s10858-019-00235-7.

Ying, J., Delaglio, F., Torchia, D. A., & Bax, A. (2017). Sparse multidimensional iterative lineshape-enhanced (SMILE) reconstruction of both non-uniformly sampled and conventional NMR data. *Journal of Biomolecular NMR, 68*(2), 101–118. https://doi.org/10.1007/s10858-016-0072-7.